Master's Thesis

Utrecht University

Faculty of Geosciences
Department of Physical Geography
Earth Surface and Water

Multi-fraction sediment sorting and entrainment at the Prins Hendrikzanddijk

Author:
Martijn klein Obbink

Supervisors:
Dr. Timothy Price
Jorn Bosma, MSc

March 27, 2022

Final version

Abstract

Since the 1990's sand nourishments are increasingly used to improve coastal safety at the wave-dominated North Sea coast. Generally, the nourished sediment is kept similar to the naturally occurring sediment and in most cases consists of well-sorted sand. However, recently, sandy beaches are also used to strengthen dykes in regions that are not wave-dominated. The Prins Hendrikzanddijk (PHZD) is an example of such a sandy retrofit, located on the leeward side of the Dutch barrier island of Texel. Additionally, a layer of coarse sediment was added on top of the PHZD in order to limit erosion. This has resulted in a complex spatiotemporally varying sediment composition in a mixed wave-current environment. It is expected that this combination of factors results in highly variable and complex sediment entrainment and transport processes, which are not yet fully understood. This research focuses on the spatiotemporally variability in the sediment composition and how this affects sediment entrainment transport at the PHZD in an aim to improve our fundamental understanding of these processes.

During a 6-week (SEDMEX; mixed SEDiments in Mixed Energy eXperiment) field campaign in early autumn at the PHZD, instruments were deployed at 6 alongshore locations, of which two had additional instruments in the cross-shore. The collected data consist of measurements on waves, currents and sediment (composition and transport). A total of 139 sediment samples were collected in the intertidal area at different cross-shore locations and over varying time intervals. Wave and current shear stresses were combined with the sediment composition to do a multi-fraction mobility analysis which is then compared to measured turbidity from Optical Backscatter Sensors (OBS).

The sediment mixture was coarse (average 1032 μm) and poorly sorted (σ_G 2.3 – 2.7) across the entire cross-shore location L2. Finer grain sizes were observed during calmer periods (430 – 850 μm) and coarser (1350 – 2000 μm) during energetic conditions. Wave related shear stresses were on average 5 times larger than that of currents. The results from the multi-fraction mobility analysis showed that the Shields number was often close to the critical Shields for incipient motion which resulted in preferential transport of the finer sediments. Over time this led to coarsening of the bed. Energetic conditions were able completely mix up the bed increasing the availability of fine sediments and flattening the beach profile. A conceptual Figure and model illustrate the how the processes affect each other and highlights how the storm frequency is an important factor in the availability of the fine sediments.

Acknowledgements

I want to begin with Dr. Timothy Price, who I would like to thank for giving me the opportunity to join this very interesting research project and the valuable feedback that he provided. Furthermore, I highly appreciate the calm and relaxed guidance he gave combined with the freedom and opportunity to let me discover my own path. I'd also like to express my gratitude to Jorn Bosma for his role as second supervisor, his extended feedback and the collaboration in the field. I am also grateful that I had such wonderful colleagues in the field, Roel Hoegen, Jelle Woerdman and Marlies van der Lugt, with whom I had a productive as well as a pleasant time on Texel. Special thanks goes to Marlies and Jelle for processing pressure and velocity data. Additionally I would like to thank the technical team, Marcel van Maarseveen, Henk Markies, Mark Eijkelboom and Arjan van Eijk for setting up all the instruments. Finally, I would like to thank my parents, Puck and friends for all the support they provided.

Contents

List of Figures

List of Tables

List of Abbreviations

ABS Acoustic Backscatter Sensor.

ADV Acoustic Doppler Velocimetry.

IPCC Intergovernmental Panel on Climate Change.

MSL Mean Sea Level.

NAP Nieuw Amsterdams Peil.

OBS Optical Backscatter Sensor.

OSSI Ocean Sensor System, Inc. Wave Gauge.

PHZD Prins Hendrikzanddijk.

RD RijksDriehoek Coordinate System.

RTK-GPS Real Time Kinematic - Global Positioning System.

SSE Sea Surface Elevation.

STM Seapoint Turbidity Meter.

TKE Total Kinetic Energy.

List of Symbols

Symbols

γ	Hiding-exposure exponent	–
ϕ_{cw}	Angle between waves and currents	°
$\rho_{s,w}$	Density of sediment/water	$\mathrm{kg\,m^{-3}}$
σ	Sediment sorting	–
τ	Bed shear stress	$\mathrm{N\,m^{-2}}$
θ	Shields parameter	–
ξ	Hiding-exposure factor	–
A_δ	Orbital excursion length	m
C_d	Drag coefficient	$0.003-$
D_*	Dimensionless particle size	–
$D_{10,50,90}$	Grain size of the th percentile	m or µm
f_g	Fraction gravel in the mixture	–
f_w	Wave friction component	–
h	Water depth	m
H_{m0}	Significant wave height	m
k	Wave number	$\mathrm{rad\,m^{-1}}$
k_s	Nikuradse roughness length	m
M_e	Mobility parameter	–
q_s	Sediment transport rate	–
r	Relative roughness	–
Re_w	Wave Reynolds number	–
s	Relative density	–

T	Turbidity	–
U	Total flow velocity	$\mathrm{m\,s^{-1}}$
U_δ	Near-bed orbital velocity	$\mathrm{m\,s^{-1}}$
v	Dynamic viscosity	$10^{-6}\,\mathrm{Pa\,s}$

Physical constants

g	Gravitational acceleration	$9.81\,\mathrm{m\,s^{-2}}$

Subscripts

c	Current-related
cr	Critical
cw	Current- and wave-related
g	Gravel
i	i^{th} grain size fraction
s	Sand
w	Wave-related

1 Introduction

River and coastal regions are the world's most densely populated areas. However, living in a coastal area also brings potential hazards such as flooding, erosion and salt intrusion. The most recent Intergovernmental Panel on Climate Change (IPCC) report emphasizes that increasing effects of climate change drive a global sea level rise and brings more extreme weather events (Masson-Delmotte et al., 2021). This emphasizes that as coastal defence was important in the past, it will still be important to continue developing coastal safety standards for the future.

In the last century, the Netherlands ensured its coastal safety with 'hard' man-made structures such as dykes and the Delta Works. Since the 1990's the Netherlands changed their coastal management strategy and applied more 'soft' nourishments at the open wave-dominated coast. With such a 'soft' nourishment sand is placed on the shoreface to ensure coastal safety under rising sea levels. In recent years this method has also been applied at locations that are not necessarily wave-dominated.

The Prins Hendrikzanddijk (PHZD) is an example of such a sandy retrofit. When in 2006 it was concluded that the Prins Hendrik dyke no longer met the safety requirements it was decided to guarantee the safety of the land in a natural way (HHN, 2017). For this, a dune-beach-spit system was built on the outside of the old dyke. This required a total of about 4.5 million m3 sand to be placed (HHN, 2017). Such a nature-based design combines coastal protection with nature development and public services (Fordeyn et al., 2020).

Situated on the sheltered east side of the barrier island of Texel, the PHZD has a mixed wave-current environment. With the dominant southwest wind direction, aeolian sediment transport is mainly alongshore to offshore directed (Strypsteen et al., 2021). In order to reduce all forms of sediment transport along the PHZD it was proposed to use an armoured layer of coarse (¿ 400 μm) material which is typically not native (Perk et al., 2019). The combination of a finer (200 μm) core and coarser armour layer results in a complex sediment mixture.

Predicting sediment transport of complex sediment in a mixed wave-current environment is extremely difficult and requires complex (numerical) models. It is important to further develop such models in order to improve predictions of sediment transport and morphological changes in the future. This could greatly help to predict when and where maintenance of such coastal interventions is required. However, our understanding of complex sediment behaviour is limited and data to validate numerical models is scarce. Improving our predictive understanding of such sandy retrofits in

general will allow further application at different locations. This study focuses on the initiation of motion of complex sediment mixtures and aims to provide useful new information and a conceptual model for sediment composition and transport.

This thesis is set-up as follows: Chapter 2 provides a theoretical background on morphology and sediment transport of mixed beds. This chapter concludes with the research objective and questions. Chapter 3 explains how this study was executed, including explanations of the six-week field campaign at the PHZD, how the data is collected and the data processing. Chapter 4 shows the results, which will be discussed in the Chapter 5. Finally, in Chapter 6 conclusions will be drawn. Any supplementary tables and figures are found in the appendices at the end of this thesis.

Figure 1: Aerial photo of the Prins Hendrik Sand dyke (Knaeps et al., 2019)

2 Background

The different physical processes, boundary conditions and their influence on the (modelling of) suspended sediment and beach morphodynamics will be discussed within the framework of the coastal morphodynamic feedback loop. All the processes in the nearshore zone are linked by a feedback loop between morphology, hydrodynamics and sediment transport (Fig. 2). The hydrodynamics drive the sediment transport which can cause a change in morphology which in turn could alter the hydrodynamics. All parts can be influenced by boundary conditions. It is important that we understand all parts of the feedback loop. This Chapter starts with an explanation of the beach morphology after which basic sediment transport mechanisms will be explained. Subsequently the influence of mixed sediments on sediment transport and sorting will be discussed. At last, a problem definition and main questions will follow.

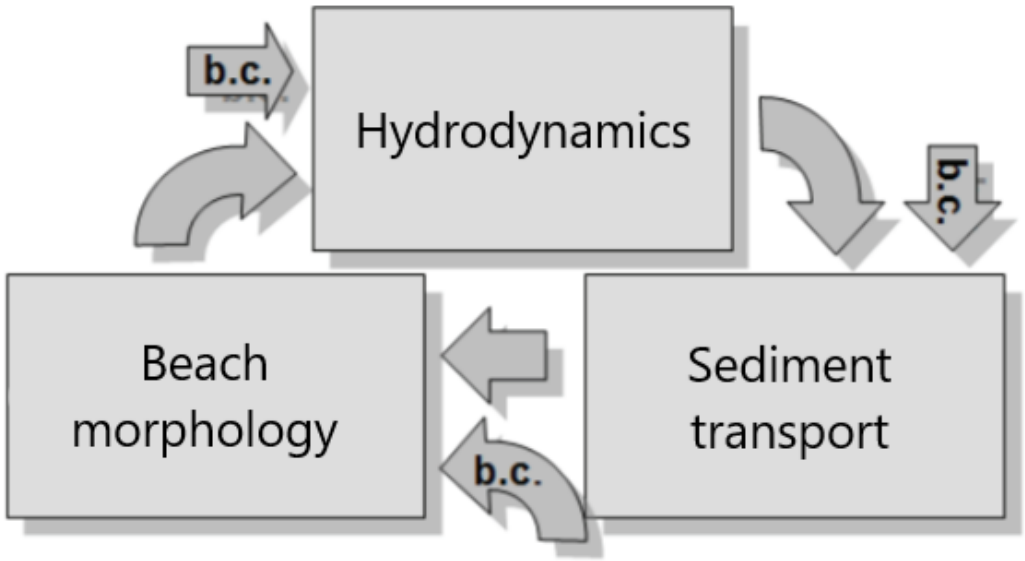

Figure 2: The coastal morphodynamic feedback loop modified after Winter (2012). b.c. are Boundary Conditions.

2.1 Beach morphology classification

The morphology of beaches can show large spatial and temporal variability. A widely used physical beach classification model is that of Wright and Short (1984). This model describes three different beach states; dissipative, reflective or one of the intermediate states. Hydrodynamic processes, sediment

transport and morphology differs significantly as a function of the beach state. Although the classification of Wright and Short (1984) is aimed towards sandy beaches, they classify coarse grained beaches as reflective. Jennings and Shulmeister (2002) further developed a classification scheme for coarse-grained beaches. This field-based classification scheme divides gravel beaches in three types based on morphodynamic properties. The three different types are shown in Figure 3 and are identified as (A) pure gravel beaches; (B) mixed sand and gravel beaches; (C) composite gravel beaches. However, it is important to note that it is possible that the three stages are part of a continuum and not necessarily three distinct types.

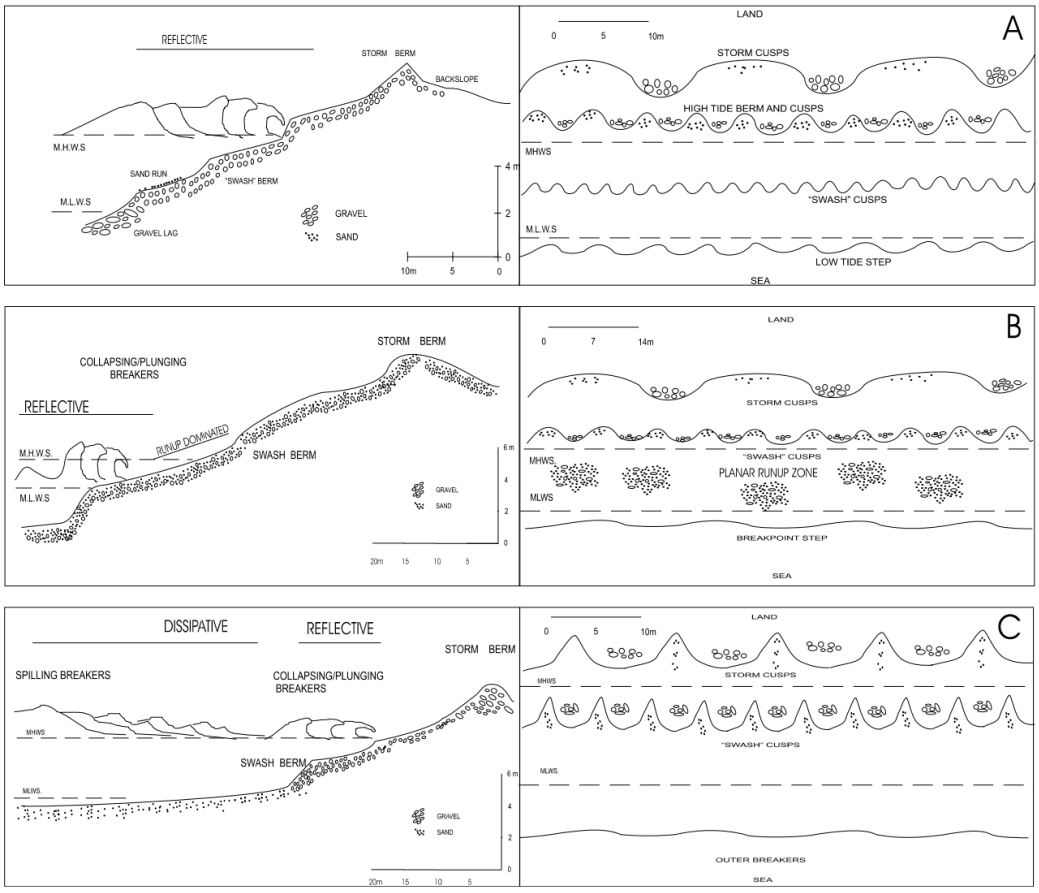

Figure 3: Schematic representation of the three gravel beach types according to Jennings and Shulmeister (2002). (A) pure gravel beaches; (B) mixed sand and gravel beaches; (C) composite gravel beaches.

The pure gravel beach has gravel throughout the whole profile and is very reflective during all tidal stages. The beach profile is steep (1:5 – 1:12.5) and cross-shore sediment sorting is common. Surf zone processes are missing and

waves are mainly surging and collapsing. Sediment transport is dominated by swash processes (Buscombe and Masselink, 2006).

The mixed sand and gravel beach is entirely composed of the mixed sediment which varies between coarse sand and pebbles. The profile has a moderate slope (1:8 – 1:25). There is a single breakpoint throughout the whole tidal cycle. Sediment is mainly transported in the swash zone. During storms the single breakpoint still exists with very little to no surf zone developments.

The composite gravel beach profiles consists of two parts, the seaward part is sand-dominated and has a lower gradient. There are spilling waves over this part of the beach with a dissipative surf zone at low tide. A distinct break in slope towards a steeper gravel-dominated part higher up the beach signifies the second part. The slopes range from 1:7 to 1:20.

2.1.1 Morphological features of coarse grained beaches

Due to the steep nature of gravel beach faces the wave breaking happens further inshore, compared to gentle-sloping sandy beaches, and is almost directly transformed to swash motion (Austin and Masselink, 2006). Therefore, cross-shore sediment transport and beach face morphology is assumed to be swash dominated. Austin and Masselink (2006) note that typical morphological features for steep swash dominated beaches are beach steps and berms, further described below.

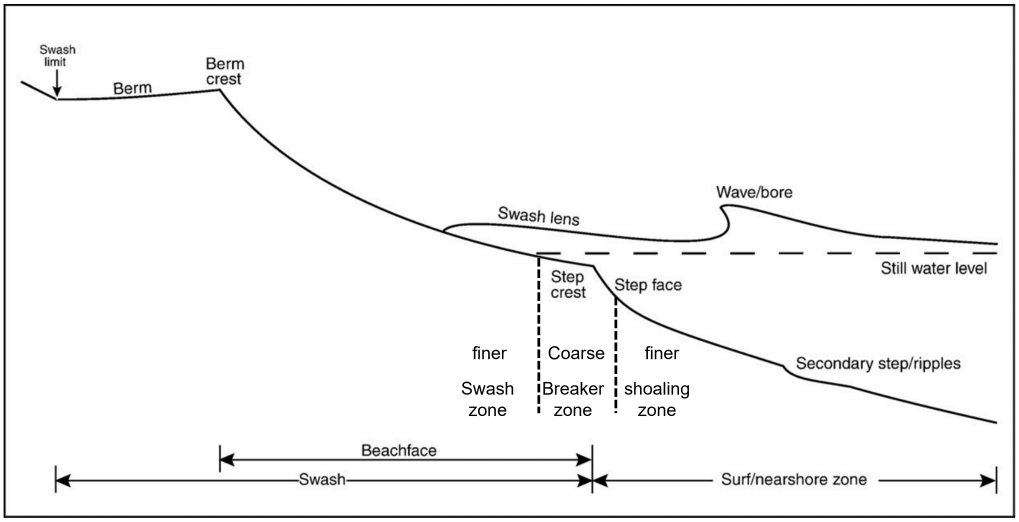

Figure 4: Morphological characteristics of a beach step (modified from Austin and Buscombe (2008))

A beach step is a morphological feature that typically has a height smaller than 0.3 m and is located at the base of the foreshore and can only exists with

breaking waves (Bauer and Allen, 1995). The beach step is the location where there is convergence between the onshore breaking waves and the offshore transport of the swash (Austin and Buscombe, 2008). Therefore the step is the location with the highest turbulence which results in the presence of the coarsest sediments as illustrated in Figure 4 (Bauer and Allen, 1995). They also mention that sometimes the only evidence of a beach step is the presence of a alongshore narrow band of coarse sediment or shell fragments located just below the Mean Sea Level (MSL). Austin and Buscombe (2008) note that the coarsening of the step is due to removal of finer sediments by preferential transport (Section 2.3.1).

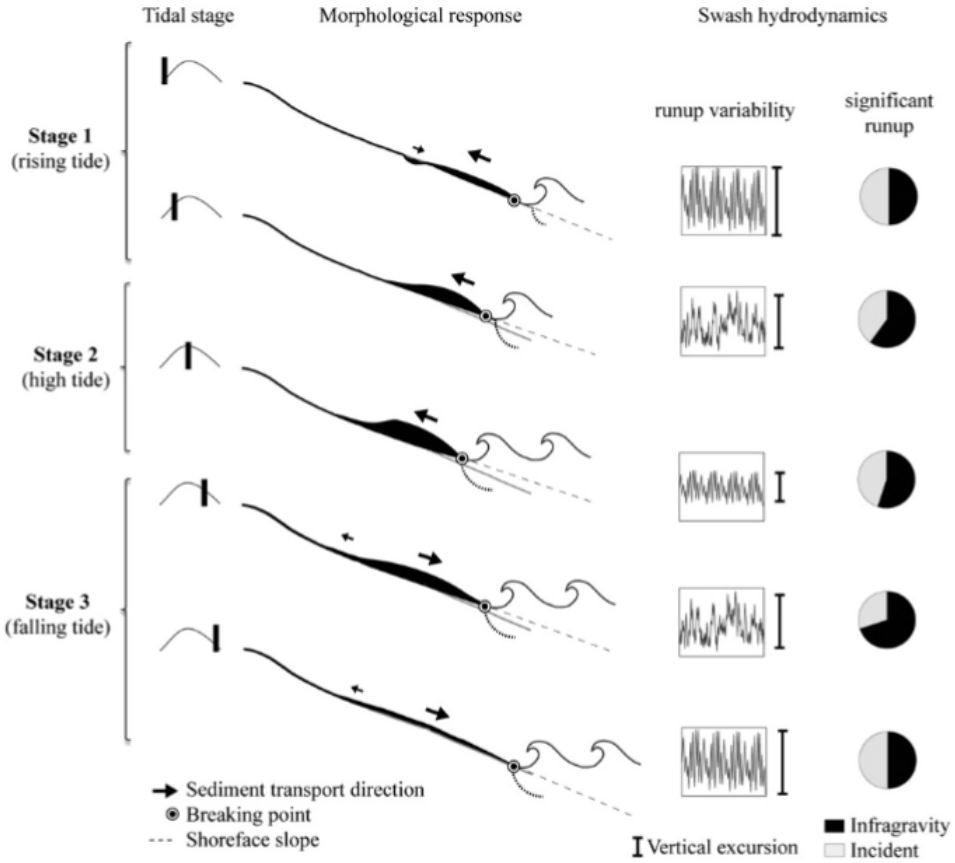

Figure 5: Morphological response to step dynamics over a tidal cycle. Figure from Almeida et al. (2015).

The breaker point of waves moves up and down the beach over the tidal cycle causing the beach step to also move up and down the beach (Austin and Buscombe, 2008). Almeida et al. (2015) found that the beach step is the main factor that controls a asymmetrical morphological response over the tidal cycle. Figure 5 from Almeida et al. (2015) shows that during the

rising tide there is onshore sediment transport which causes berm formation and a decrease in the beach slope and reduce the run-up energy. During the falling tide there is sediment erosion again due to remobilization of the step deposits which increases the beach slope and run-up energy. Observations during energetic conditions show that the reflective characteristics shift towards deposition in the lower foreshore due to growth of the beach step (Poate et al., 2013). They also show that it results in reduced run-up due to increased wave dissipation in the lower foreshore.

The asymmetrical swash processes controlled by the beach step create a berm. This is a wedge shaped depositional morphological feature close to the high water line (Bendixen et al., 2013). Apart from the beach step, further contributions to asymmetrical swash processes on gravel beaches is infiltration. The backwash is weakened due to infiltration into the coarse sediments causing sediments to settle near the maximum run-up which results in vertical accretion (Austin and Masselink, 2006; Austin and Buscombe, 2008; Masselink et al., 2010). The berm height is dependent on the wave run-up, which results in the 'berm height paradox'. Higher offshore waves result in higher run-up which allows the berm to grow, yet the largest waves will also erode the berm (Weir et al., 2006; Bendixen et al., 2013). Erosion of the berm during the falling tide is not always significant due to spring-neap variations in the tide. The conceptual model of Weir et al. (2006) shows that berm heights can vary over the spring-neap cycle (Fig. 6). In this model the slope directly after an erosional event is more gentle (a). Following, there is vertical growth of the berm and a steepening of the beach (b). During neap-tide there is more horizontal progradation of the berm as water levels are not high enough for overtopping (c). During spring tide the sediment deposited during neap tide is moved up the berm crest causing vertical growth of the berm (d).

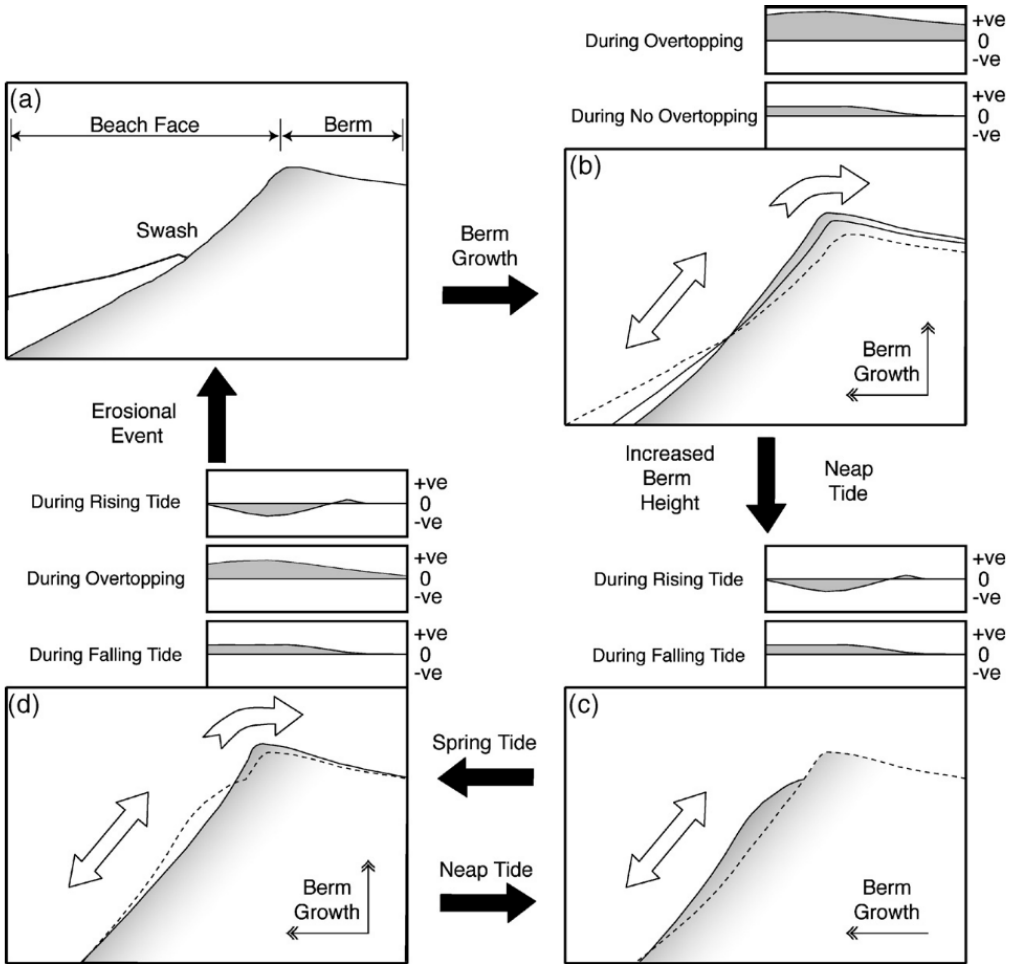

Figure 6: The four stages of the conceptual model for berm growth according to Weir et al. (2006).

2.2 Sediment transport

Sediment can be transported in roughly two ways. Bed-load transport, which is the sediment transport in a thin layer (0.01 m) above the bed and suspended sediment transport which consists of sediment transported above the bed-load layer (Van Rijn, 2007*a*). Usually suspended sediment transport is the prevailing mode of transport in low energetic conditions (Van Rijn, 2007*b*). This section describes the sediment transport by waves and currents.

2.2.1 Sediment entrainment

An important factor in sediment transport is the incipient motion of sediment. Sediment is entrained when the fluid forces acting on the sediment is larger than the resisting forces (Van Rijn, 2007*a*). Figure 7 gives a visual representation of the force balance in which the drag and lift forces cause entrainment while the gravitational force is the resisting force. The threshold of sediment motion is often based upon shear stresses in uniform flow conditions. The most widely used theory is that of Shields (1936), who expressed the critical condition in terms of the dimensionless Shields number (θ). Shields (1936) used the (θ_{cr}) as a function of the grain Reynolds number (Re). θ is a dimensionless function of the shear stress, sediment particle density, fluid density, gravitational acceleration and the sediment particle diameter.

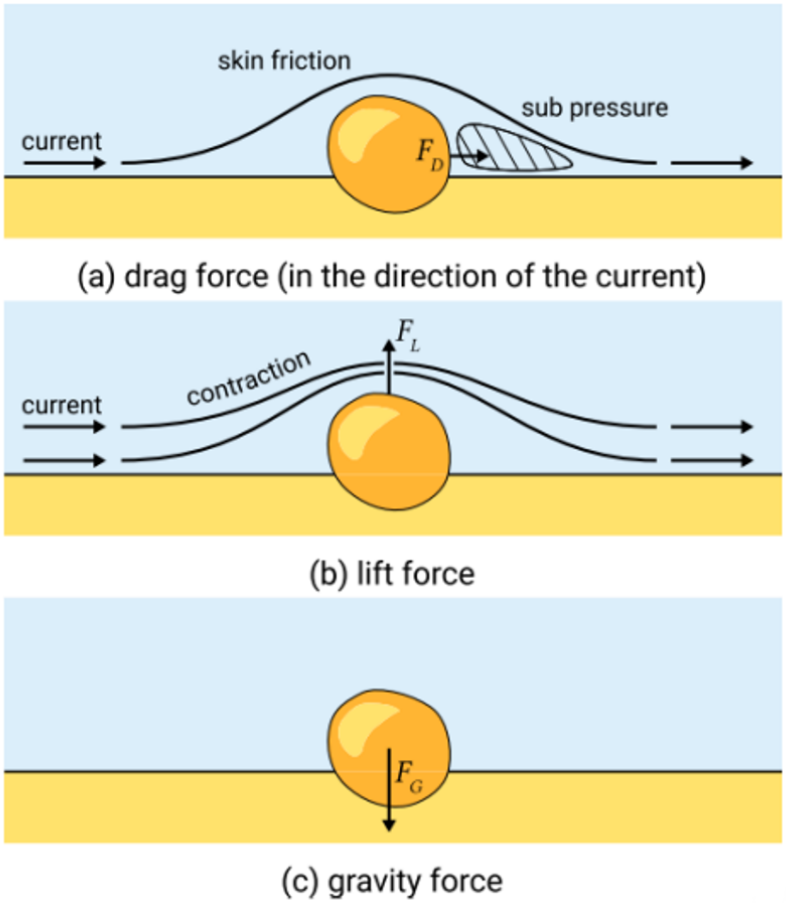

Figure 7: The drag (a), lift (b) and gravitational (c) forces acting on a particle. Figure from Bosboom and Stive (2021)

For incipient motion under waves the Shields curve was extended to also fit wave or wave-current data (Madsen and Grant, 1977; Soulsby et al., 1997). Van Rijn (1993) shows that θ can be used under combined wave-current conditions when the wave period-averaged absolute bed shear stress is used. A less frequently used approach is a more empirical relationship in which incipient motion of waves and currents is expressed in a critical velocity, critical shear stress or critical wave height (Bagnold, 1946; Madsen and Grant, 1977; Dou et al., 2001).

An important difference between currents and waves is the different turbulence structure and boundary layer (Zuo et al., 2017). Apart from the normal drag force waves also exhibit extra wave inertia force in oscillatory flow in the onshore phase of waves due to skewness and wave shape asymmetry (Nielsen, 1992; Foster et al., 2006). Ruessink (2010) shows that wave breaking is the dominant source which generates turbulence for the cross-shore shear stress. Furthermore, Aagaard and Hughes (2010) showed that the type of wave breaking affects the suspended sediment concentration as plunging breakers played a more significant role in sediment entrainment than spilling breakers and shoaling waves.

2.3 Mixed sediments

There are several studies that confirm that the sediment can vary in spatial and temporal scales. For example Holland and Elmore (2008) found that simplifying coastal sediments into a single D_{50} value does not capture the influence of many coastal sediments. Furthermore, Gallagher et al. (2011) found that the grain size of beach slopes can spatially vary in the order of 0.2-0.7 mm over just 10-100 m. Knowledge on sediment dynamics is even more important when a mixed sand-gravel sediment composition is present, as it results in differentiated transport and sorting. When considering mixed sediments, the dynamics of individual grains can only be acquired in the context of the background population. In other words, information on the whole sediment mixture is necessary in order to determine when a single grain is mobilized.

2.3.1 Transport sorting

Spatial variability of the sediment distribution is often a result of sediments responding differently to similar hydrodynamic conditions (Richmond and Sallenger Jr, 1985). This can result in fining in offshore direction as often found at the sandy Dutch coast (Guillén and Hoekstra, 1996; Hassan, 2003). Furthermore it can also result in longshore variations in grain size as

found at the Sand engine (Huisman et al., 2016). The most relevant sorting processes are settling and entrainment which together results in transport sorting (Slingerland and Smith, 1986).

Sorting due to preferential entrainment is the mechanism where smaller size fractions are brought into motion while the shear stresses are to weak to bring larger grains into motion, resulting in a coarsening of the bed (Huisman et al., 2016). This is especially the case for environments that are close to the critical bed shear stresses of the finer sediments (Komar, 1987), which is illustrated Figure 8.

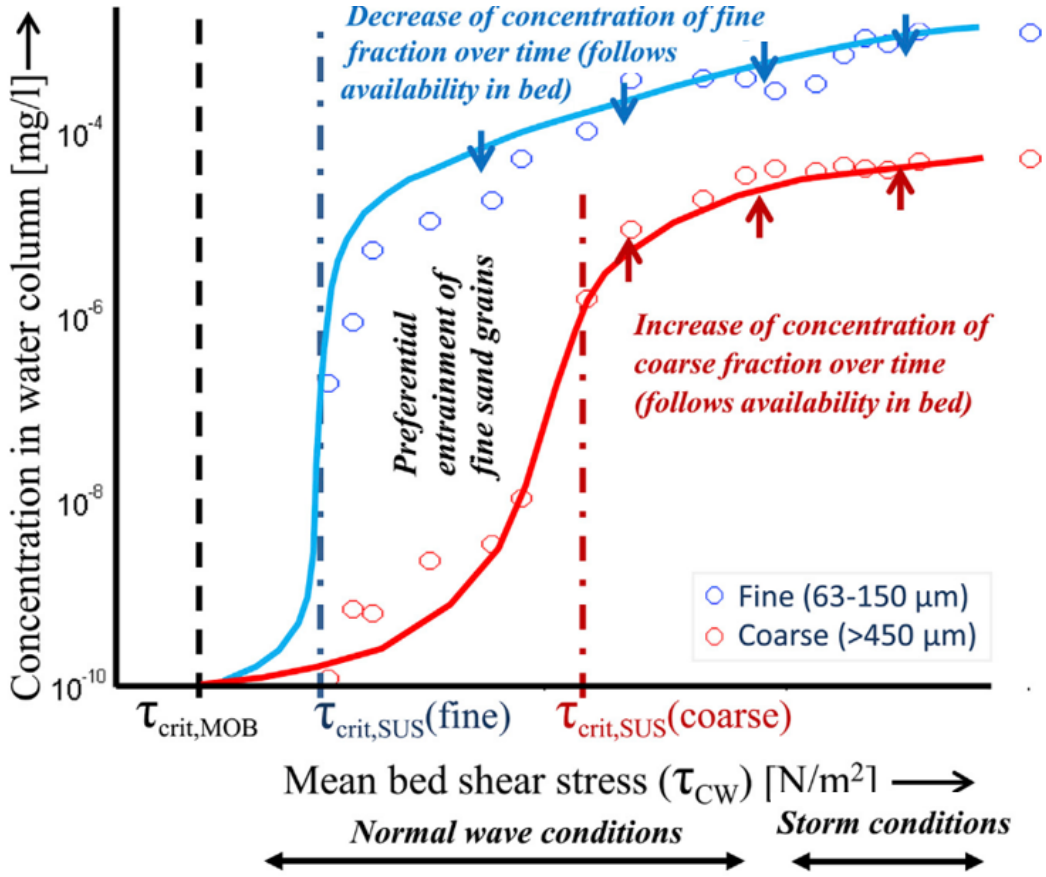

Figure 8: Measured suspended sediment concentration against mean bed-shear stress indicating a preferential transport of finer sediments. Vertical dashed lines indicate the critical value for mobility, suspension of fine sediment and suspension of coarse sediment. Figure from (Huisman et al., 2018).

After the particles are entrained, they are subsequently transported by the mean current. Settling of sediment occurs when the buoyancy force drops below the entrainment threshold due to a reduction in turbulence (Van Rijn,

2007*a*). An important parameter is the settling velocity which specifically plays a role when dealing with mixed sediments in environments where finer grains are transported over greater distances than coarser grains (Baba and Komar, 1981). This is described by the settling velocity, which is a function of the sediment density, size, shape and angularity (Rieux et al., 2019). The settling velocity of spherical particles range from 0.01 – 1 $\mathrm{m\,s^{-1}}$ for grain sizes of 100 – 1000 μm respectively (Li et al., 2020). For shell fragments of 6000 μm the settling velocity can vary between 0.066 – 0.2 $\mathrm{m\,s^{-1}}$, which is significantly lower compared to spherical particles (Rieux et al., 2019). A more angular and lighter particle thus settles slower than a well rounded more dense particle. The settling velocity is also important in case of flow reversal. Sediment with a high settling velocity is expected to be transported onshore under waves, as it settles before flow reversal while sediment with a lower settling velocity can be transported offshore as it settles after flow reversal (Christensen et al., 2019). Furthermore, Moss (1963) introduced the concept of acceptance and rejection in the swash zone of mixed sediments. In this settling process smaller grains are accepted in by the larger background grains (kinematic sieving) while larger grains pass over. The combined effect of preferential entrainment and settling result in preferential transport of finer sediments.

2.3.2 Hiding-Exposure effects

However, in mixed beds hiding-exposure mechanisms can reduce preferential entrainment as finer grains 'hide' between the larger grain (Fig. 9). For bimodal sediments this limits the mobility of smaller grains by up to 64 % and enhances the mobility of larger grains by up to 75 % due to increased exposure (McCarron et al., 2019). In other words, when sediment is fully mixed, this result in a higher critical bed shear stress for the smaller grains and a lower critical bed shear stress for the larger grains. This is further illustrated in Figure 9, in which the hiding exposure effect in relationship to sediment composition is shown. To determine the critical bed shear stress for different grain sizes including the hiding-exposure effect, there are several methods. One method uses a correction factor for incipient motion which is multiplied by the $\theta_{cr,D50}$ to calculate the $\theta_{cr,i}$ (Egiazaroff, 1965; Wilcock and Crowe, 2003). Another method is to estimate the bed shear stress exerted on each grain size fraction (van der A et al., 2013). Further incorporation of the hiding-exposure effect in sediment entrainment can be found in Section 3.3.5.

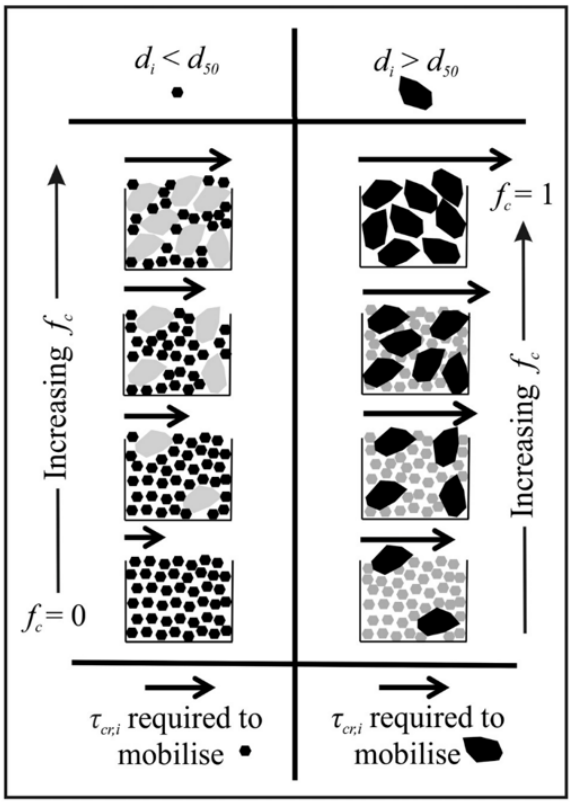

Figure 9: The critical bed-shear stress for initiation of motion revealing the hiding exposure effect. f_c is the fraction of coarse sediment in the mixture. Figure from McCarron et al. (2019).

2.3.3 Armouring

When small grains are removed due to preferential transport (Section 2.3.1) a relative homogeneous layer of coarse sediment remains. Shell (fragments) can also act as an armour layer (Miedema and Ramsdell, 2011). According to Diedericks et al. (2018) the critical bed shear stress of shell fragments can be 2.69 to 9.81 times larger than grains of 900 μm and 300 μm respectively. Bed armouring causes a reduction in the depth of the active bed layer, which is the layer in which particles are potentially mobilized (Reed et al., 1999). Therefore, the armour layer limits the mobilization of the grains beneath, reducing sediment transport (Van Rijn, 2007*c*). A recent study of Rafati et al. (2020) shows that bed armouring is especially dominant in low oscillatory flow velocities, while in increased flow velocities the bed becomes mixed again resulting in hiding-exposure effects to be more dominant, which increases the mobility of coarser grains (Section 2.3.2).

2.4 Problem description

Since the 1990's sand nourishments are increasingly used in Dutch ocean management to increase coastal safety at the wave-dominated North Sea coast (Brand et al., 2022). Over the last decade, sandy beach nourishments are also used to strengthen dykes, such as the Hondsbossche dunes, but also in regions that are not always wave-dominated. The PHZD is an example of such a sandy retrofit. The mixed wave-current environment can cause variability in the sediment transport directions and magnitudes in both the longshore as the cross-shore directions. In addition to that, the mixed sediment composition of the beach further complicates sediment transport predictions and requires complex (numerical) models. It is difficult to predict when and why conditions are favourable for the sediment to get into motion.

2.4.1 Research questions

This thesis aims to answer to following research question: **Under which conditions is the complex sediment mixture transported in suspension in the mixed wave-current environment of the PHZD?** To answer this, two questions, both subdivided into 3 sub-questions, are formulated:

1 What is the sediment composition and how is it sorted?

(a) *What are the different cross-shore sediment grain sizes?*

(b) How is the sediment sorted in the cross-shore?

(c) How does the sediment sorting vary over time?

2 What hydrodynamics drive the suspended sediment transport and how is this affected by the grain size distribution?

(a) *Is the stirring of sediment primarily wave- or tide-driven?*

(b) How does the mixed grain size mixture control the mobility of the sediment?

(c) How is the morphology shaped by the sediment composition?

In this project I will investigate the sediment composition and transport across the intertidal zone of the PHZD. To answer these questions, a fieldwork campaign was organised at the PHZD, during which the hydrodynamics and suspended sediment transport in the intertidal area is measured at six alongshore locations (of which two more extensively) and along one cross-shore profile. By calculating the Shield parameter for the various sediment

compositions over time it is attempted to gain more understanding of the stirring and transport of complex sediment mixtures in a mixed wave-current environment and how this relates to the beach morphology.

Hypotheses

1 (a) The grain size is expected to resemble the sediments deposited during the construction of the PHZD.

(b) The sediment is expected to be fining in offshore direction as generally found in sandy coastal areas (Guillén and Hoekstra, 1996; Hassan, 2003). In general the sediment composition is expected to be poorly sorted due to the armour layer. Furthermore it is expected that a beach step is present which will also be visible in the sediment composition as a coarser layer around the lower foreshore (Bauer and Allen, 1995; Austin and Buscombe, 2008).

(c) The sediment composition is expected to vary during the different conditions. During calm conditions the sediment is expected to be finer. However, depending on whether currents alone can mobilize the sediment, preferential transport as explained by Huisman et al. (2016) could lead to coarsening of the bed. Furthermore the sediment composition is expected to be coarser during energetic storm conditions.

2 (a) The sediment is expected to be stirred by waves. This is due to the fact that breaking waves create turbulence which exhibits extra inertia force (Nielsen, 1992; Ruessink, 2010; Zuo et al., 2017).

(b) The mobility is expected to be influenced by the hiding-exposure effect (McCarron et al., 2019) and armouring by shells (Miedema and Ramsdell, 2011; Diedericks et al., 2018) and coarsening of the bed due to preferential transport of finer sediments (Huisman et al., 2016; Rafati et al., 2020).

(c) The slope of the beach is expected to be relatively steep due a relativly coarse mixed sediment mixture. This would also result in morphological features related to gravel beach types such as berms and beach steps (Jennings and Shulmeister, 2002; Austin and Buscombe, 2008).

3 Methods

The basis for this research lies within a 6-week (SEDMEX; mixed SEDiments in Mixed Energy eXperiment) field campaign at the PHZD, conducted from 9 September to 19 October 2021. During this period researchers from the TU Delft and Utrecht University collaborated on gathering data on waves, currents and sediment (transport). The aim of this field campaign was to find the sedimentary dynamics in a mixed wave-current environment.

3.1 Site description

The study site is the PHZD located on the sheltered south-east side of the barrier island Texel (Fig. 10). The PHZD is built on the Schanserwaard shoal, which is 1.4 to 2 m below MSL. The Schanserwaard shoal is bordered by the PHZD on the north-west sides and the Texelstroom on the south-east side. The PHZD is a sandy retrofit which has a dune-beach-spit system design that was completed in 2019.

3.1.1 Morphology

The new dune is partially built on the old Prins Hendrik dyke and its primary vegetation is Marram grass. The south part of the 3.5 km long beach-spit system has a southwest to northeast orientation of $\sim 39°$, while the spit extends in a slightly more easterly direction of $\sim 51°$. The beach at the south part is ∼80 m wide while the spit is ∼180 m wide (Fig. 10). Along the beach-spit system several natural windscreens are placed at which sediment accumulated to prevent further aeolian transport. A layer of coarse grains and shells (Section 3.1.2) is placed on top of the beach-spit system to further reduces aeolian and coastal transport. The research focuses on the intertidal area which by design had a slope of 1:50 (Perk et al., 2019). The intertidal area is 15 to 30 m wide (Fig. 10).

The PHZD shows alongshore variation in cross-shore profiles. The spatial variability of the beach morphology is shown by plots of measured bed profiles for all six locations (Fig. 10 b–g). Morphological features like beach step, bar and berm will be identified for L2. The turning point between erosion and accretion is at +0.3 m Nieuw Amsterdams Peil (NAP). The average slope of the intertidal area between -1 and +1 NAP is calculated and shown in Figure 10. The average slope of the intertidal area is steeper at the spit (L1 – L4) and a lot more gentle at L5 and L6.

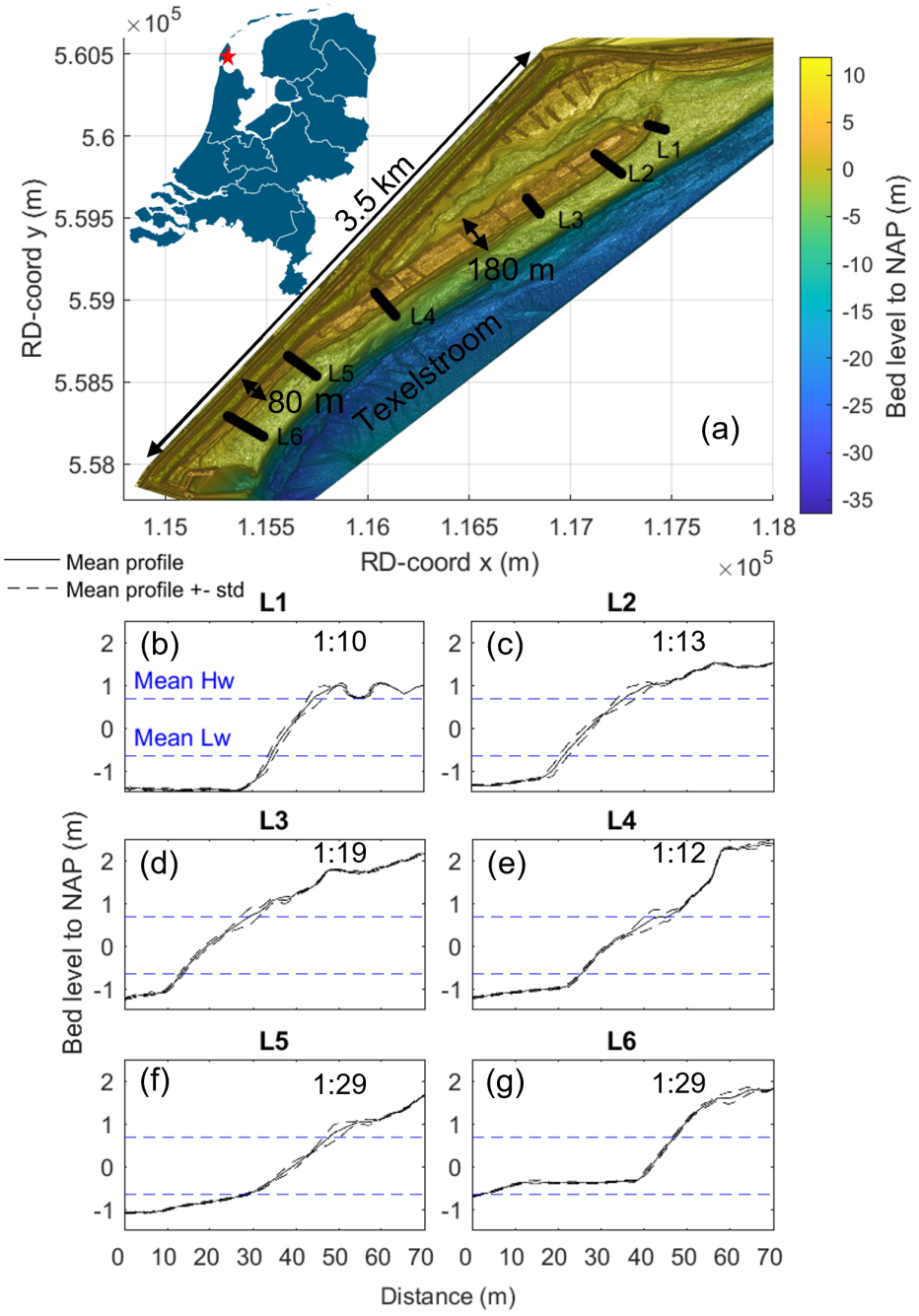

Figure 10: (a) The location of the Prins Hendrik Sand dyke and the six cross-sections (b – g) of the longshore instrument locations. Indicated within the cross-sections is the average slope during the campaign between -1 and +1 m NAP.

3.1.2 Original grain sizes

Two sand extraction areas in the North Sea were used for the construction of the PHZD by the contractor Jan de Nul. In both extraction areas the sediment consisted of three typical grain sizes. An overview of the grain size classes can be found in Table 1. Sand with grain sizes from 200 - 400 μm was used for building the sand dyke while the beach was covered with 30 cm of the very fine gravel (400 – 2000 μm).

Location	**Size class**	**Terminology (Jan de Nul)**	**Terminology (Friedman & Sanders (1978))**
Q2N	D_{50} <220 um	Finest	(very) Fine sand
	D_{50} >220 um	Fine	Fine sand
	D_{50} >280 um	Medium	Medium sand
L15	D_{50} >280 um	Medium	Medium sand
	D_{50} >400 um	Coarse	Medium or coarse sand
	D85 >2000 um	Very coarse	Very fine gravel

Table 1: Sediment grain size classes from the extraction areas according to Jan de Nul and the descriptive terminology according to Friedman et al. (1978)

3.1.3 Wind, waves and currents

The tidal range is about 1.4 m, at the Marsdiep inlet the tidal asymmetry is flood dominant with tidal velocities that can reach up to 1.8 m s^{-1} (Buijsman and Ridderinkhof, 2007). Waves from the North Sea have a significant wave height (H_{m0}) of 1.3 m and storm waves can be over 6 m (Elias et al., 2006). However, almost all waves from the North Sea break over the ebb tidal delta. Local waves are fetch limited and can be up to 2 m (Elias et al., 2012).

Conditions during the campaign

Figure 11 shows the conditions during the campaign measured at L2. The H_{m0} is closely related to the wind speed in combination with a (cross) onshore direction (Woerdman 2022). The conditions can be divided into 5 periods, described below. The first week from 11 to 18 September was very calm with a H_{m0} of 0.1 – 0.15 m and is referred to as the calm period. From 19 – 20 September wave heights increased to 0.15 – 0.45 m. From 21 – 26 September it was relatively calm again with H_{m0} of 0.1 – 0.25 m. Following is a period from 27 September to 5 October with stronger winds and higher waves up

to 0.5 m and is referred to as the storm period. Then from 6 to 18 October the conditions are calm again with H_{m0} of 0.1 – 0.2 m. Current velocities on the shoal range from 0.2 to 0.4 m s^{-1}, which is significantly lower than in the Texelstroom (Section 3.1.3). For more information and a detailed analysis of the hydrodynamic conditions I refer the interested reader to Woerdman (2022).

3.2 Data acquisition

During the field campaign various instruments were deployed. Instruments were placed at six locations along the beach, named L1 - L6, where L1 is at the end of the spit (Fig. 10). Two cross-shore arrays were installed at L2 and L4. The cross-shore locations within each of these arrays are referred to as C1 to C10, where C1 is the most landward location (Fig. 12). This study focuses on the cross-shore array at L2 (Fig 10).

3.2.1 Bed levels

During the field campaign a Real Time Kinematic - Global Positioning System (RTK-GPS) was used for measuring the bed elevations. The RTK-GPS has a horizontal accuracy of 0.02 m and 0.03 – 0.05 m in the vertical direction. As the beach is a dynamic environment, the bed (level) is prone to changes. As a result, the height of a sensor above the bed is variable over time. To account for that, the height of every instrument above the bed was measured periodically with both a ruler and the RTK-GPS. At the start of the campaign it was done every day, this later changed to every two to three days. Furthermore, the instruments were checked for sea grass and barnacles, which were removed if present. During the same periodical checks the RTK-GPS was used to measure the cross-section of the beach profile along the six along-shore instrument locations in order to monitor any changes in the beach profile.

3.2.2 Wind, waves and currents

Data on wind speed and directions were retrieved from weather station De Kooy near Den Helder. It consists of 10-minute data collected at a height of 10 m. The weather station is approximately 10 km from the PHZD. Strypsteen et al. (2021) showed that the wind velocities can be slightly different between the two locations. They show that offshore winds and onshore winds can be up to 10% lower and 40% higher respectively. Local variations in air

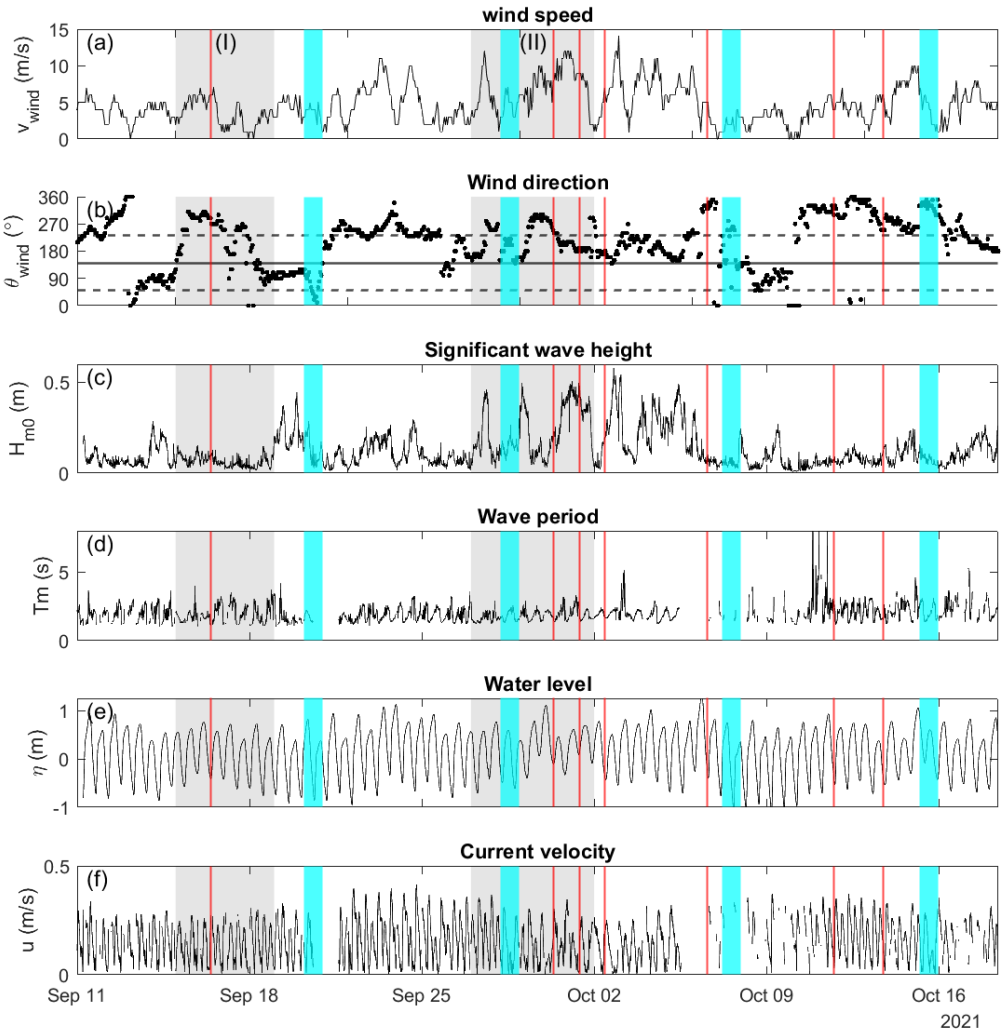

Figure 11: Conditions during the campaign, wind speed is measured at the Kooy and the rest is measured at L2. (a) The wind speed in m/s, (b) the wind direction in degrees North, (c) the significant wave height, (d) the wave period, (e) the water level and (f) the current velocity. Vertical red lines indicate single sample moments while the cyan colored area indicate time periods in which a full tidal cycle is sampled (Section 3.2.4). The gray areas indicate the calm (I) and storm (II) period used further in this thesis.

pressure was measured at L2 at a height of 2 m NAP using a KELLER barometric pressure sensor.

Pressure and current data are collected on several cross-shore locations at L2. During this study mainly data collected at L2C10 (Fig. 12) was used, at this location the bed level was -1.45 m NAP. The waves were measured using

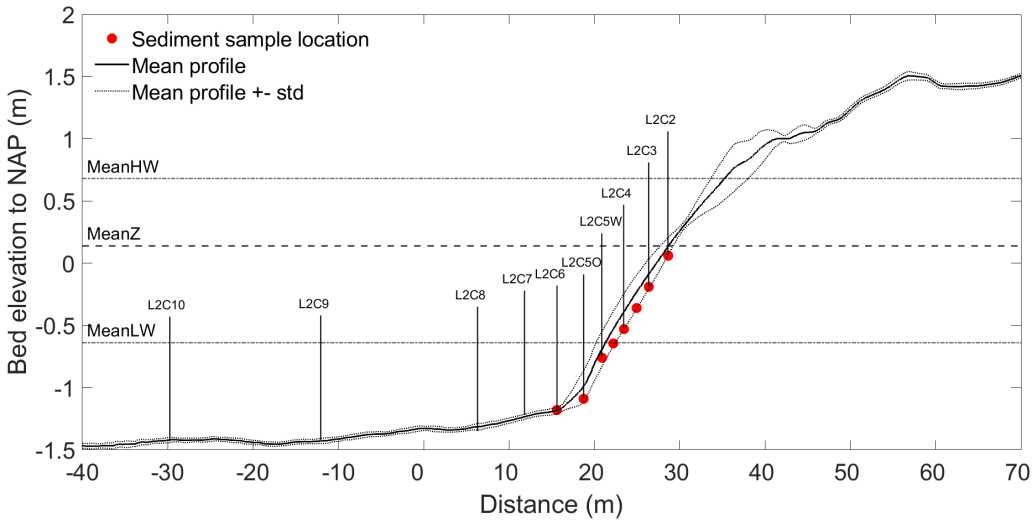

Figure 12: Set up of the instrument locations across profile L2.

a Ocean Sensor System, Inc. Wave Gauge (OSSI) positioned approximately 50 cm above the bed. The wave gauge was continuously measuring at a frequency of 10 Hz and with an accuracy of 1 mbar. For current data at L2C10 a Nortek Acoustic Doppler Velocimetry (ADV) was used, which had its measurement volume around 15 cm above the bed. The velocity was continuously sampled at a frequency of 16 Hz. A pressure sensor and three SONTEK ADV's were also deployed at location L2C5 which were not used due to processing issues (Section 3.3.2). Deployment details of all instruments used in this study is also summarized is in Table 2 while Figure 13 shows pictures of all instruments in the field.

Location	**Instrument**	**Depth (m NAP)**	**Height above bed (m)**	**Frequency (Hz)**
L2C5	Sontek ADV	-0.85	0.15, 0.40, 0.70	10
L2C5	Pressure sensor	-1.10	0	4
L2C5	STM	-1.10	0.40, 0.75	4
L2C5	STM array	-1.10	0.05	4
L2C10	Nortek ADV	- 1.45	0.15	16
L2C10	OSSI Wave Gauge	- 1.45	0.50	10

Table 2: Deployment details of instruments used during this study.

3.2.3 Sediment transport

For this study suspended sediment transport was measured using Seapoint Turbidity Meter (STM)'s at cross-section L2 at location C5. Three STM's were placed at a bed level of $\sim$ -0.75 m NAP. This is shown at the top of Figure 13. At $\sim$ 5 cm above the bed an STM array was placed, one device consisting of 5 STM's placed right on top of each other. Above the STM array two more STM's were placed at $\sim$ 40 and $\sim$ 75 cm above the bed. All OBS sensors attached to the frame were measuring with a sample frequency of 4 Hz (Tab. 2).

A STM is an Optical Backscatter Sensor (OBS) that indirectly measures suspended sediment concentration. The instrument emits near-infrared light (λ = 0.780-0.865 μm) that is back-scattered by suspended particles which is then registered by the sensor (Pearson et al., 2021). A drawback of the OBS is its sensitivity to different particle sizes. Pearson et al. (2021) mentions that back scatter is strongest when the particle size is similar to the emitted wavelength, which makes OBS sensors more sensitive to very fine particles (1 μm).

3.2.4 Sediment composition

Mixed sediment samples were taken at several days during the campaign at the alongshore locations L1 – L6. As this thesis focuses primarily on cross-section L2, the along-shore sediment samples are neglected for now. Along L2 samples were taken at eight different locations which are shown as red dots in Figure 12. These locations correspond to the locations of L2C2 to L2C6. Extra samples were taken between L2C3 and L2C4 (L2C3.5) and L2C4 and L2C5 (L2C4.5). As the L2C5 frame was bigger, samples were taken at both sides of the frame named L2C5W (for West) and L2C5O (for Oost (east)).

Sediment samples were taken on 11 different days during various conditions, the red and cyan vertical lines in Figure 11 show when the samples were taken. The red lines indicate single samples taken during low tide at L2C3 and L2C5W. The cyan lines indicate periods where sediment samples were taken during a full tidal cycle. During such a day, samples were obtained at all eight cross-shore locations at low-tide, high-tide and both ascending and descending mid-tides. Giving a total of 8*4 (32) samples per tidal cycle. This happened twice at spring-tide, and twice at neap-tide. Furthermore, eight samples were taken at low-tide storm conditions on the first of October. Table 3 summarizes the sediment sampling details.

Samples were taken using a small jar with a diameter of $\sim$5 cm. The jar was carefully pushed into the sand until a depth of approximately 5 cm.

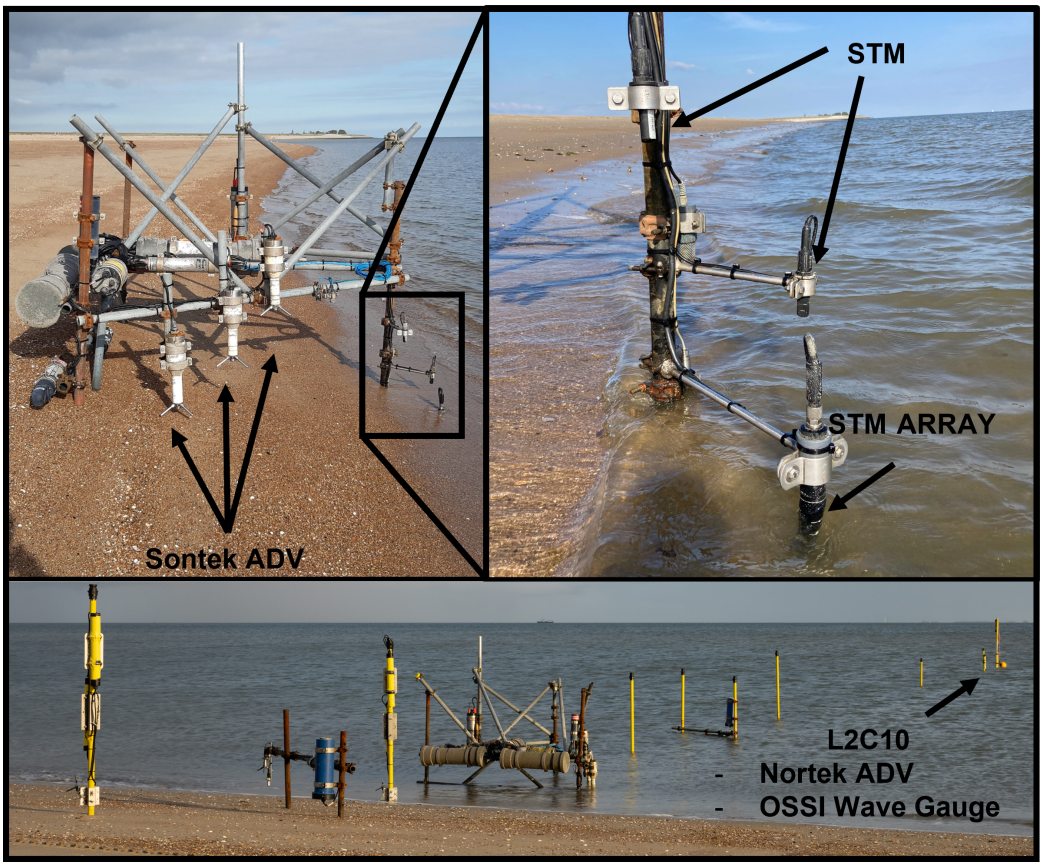

Figure 13: Top: Frame located at L2C5 with three Sontek ADV's, two STM's and an STM array. Bottom: The entire cross-shore array of L2 with the ADV and OSSI at L2C10 indicated.

When taking the jar out, we used our hands to make sure no sediment fell out. The sample was then put in labelled resealable plastic bags.

3.3 Data processing

3.3.1 Bed levels

The RTK-GPS data is projected on a RijksDriehoek Coordinate System (RD) 2008. Outliers were manually removed through visual inspection of the data. These are generally data points with a large offset in elevation for 1 or 2 consecutive points. This can be explained by the occasionally poor connection of the RTK-GPS.

Not every transact is measured at the exact same location (Fig. 14 a). To enable the direct comparison between transacts, it is necessary that the

Date	Timing	Locations	Number of samples
16-09	Low tide	C3, C5W	2
20-09	Full tidal cycle, spring	All	31
28-09	Full tidal cycle, neap	All	32
30-09	Low tide	C3, C5W	2
01-10	Low tide	All	8
02-10	Low tide	C3, C5W	2
06-10	Low tide	C3, C5W	2
07-10	Full tidal cycle, spring	All	32
11-10	Low tide	C3, C5W	2
13-10	Low tide	C3, C5W	2
15-10	Full tidal cycle, neap	All	23

Table 3: Sediment sampling details. All locations correspond to the 8 sampling locations in cross-shore array L2.

transects are projected to the same straight line. For this, every point of every line is projected on a linear trend line fitted through all transects per cross-section L1 - L6. The bottom part of Figure 14b shows that the distance between two points slightly changes due to the projection, it is always slightly shorter. However, the effect of this is supposed to be very minimal and is thus ignored. For visualization the transects are rotated to 2D.

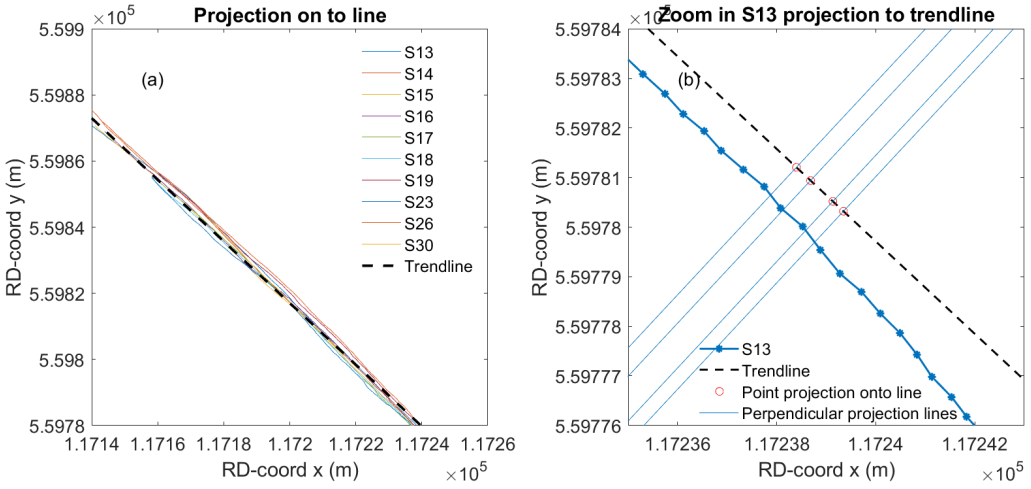

Figure 14: All measured transects of L2 projected onto a trend line. Left panel (a) shows the deviations between each transact and the linear fitted trend line. The right panel (b) shows for four points of the line, the projection on the trend line works.

The cross-shore profile of L2 was used to track changes in the bed profile and temporal variability in morphological features. This was done by linear interpolating the cross-shore profiles. These were used to identify periods of erosion or deposition of sediments. There is extra focus on the bed elevation at the sensor locations. The result will create a increased understanding of flow and grain size patterns using the morphology.

3.3.2 Hydrodynamic base-parameters

The pressure and current data was carefully calibrated, validated and processed in 10-minute blocks by Woerdman (2022). The pressure sensor was corrected for atmospheric pressure using the KELLER and subsequently checked for exposure to air. Linear wave theory was used to convert the pressure data to Sea Surface Elevation (SSE). Pressure fluctuation from wind-driven or tidal circulation was eliminated using a high-pass (0.05 – 1.00 Hz) filter on the SSE. Subsequently, the SSE is used for calculation of the non-directional spectral density (S) and the H_{m0}, which was calculated as:

$$H_{m0} = 4 * std(SSE) \tag{1}$$

The near-bed orbital velocity (U_δ) was calculated using the method of Wiberg and Sherwood (2008):

$$U_\delta = \sqrt{2 \sum S_u \; df} \tag{2}$$

In which S_u is the bottom spectral density which can be calculated by:

$$S_u = \frac{\omega^2}{sinh^2(kh)} S \tag{3}$$

in which ω is the radian frequency, k the wave number and h the water depth.

For the current velocity, data periods when the instruments were not submerged were also excluded. Following, the data was despiked using the method of Goring and Nikora (2002); Elgar et al. (2005); Mori et al. (2007). For the beam correlation a threshold of 70% was used. The measured velocity was converted to East (u), North (v) and Up (w) velocities. A combined current velocity (U) was calculated by Pythagoras theorem:

$$U = \sqrt{u^2 + v^2} \tag{4}$$

Due to difficulties with the processing of data collected at the L2C5 frame data from L2C10 was used (Fig. 12). One of the difficulties arose due to the fact that the sensors at L2C5 were regularly above the water, leaving little data. Furthermore, large bed level changes at L2C5 further complicated

processing. For the periods where H_{m0} processing was possible at L2C5, this was compared with data from L2C10 (Fig. 15). This shows that the H_{m0} at L2C10 is slightly larger. Especially for waves larger than 0.3m L2C10 was larger about 10% higher. This could be due to the fact that there is some wave dissipation over the shoal from L2C10 to L2C5 when there were larger waves. However, the correlation of 0.86 (R^2) and Root mean Square Error (RMSE) of 0.03 m is considered sufficient for further analysis of sediment entrainment.

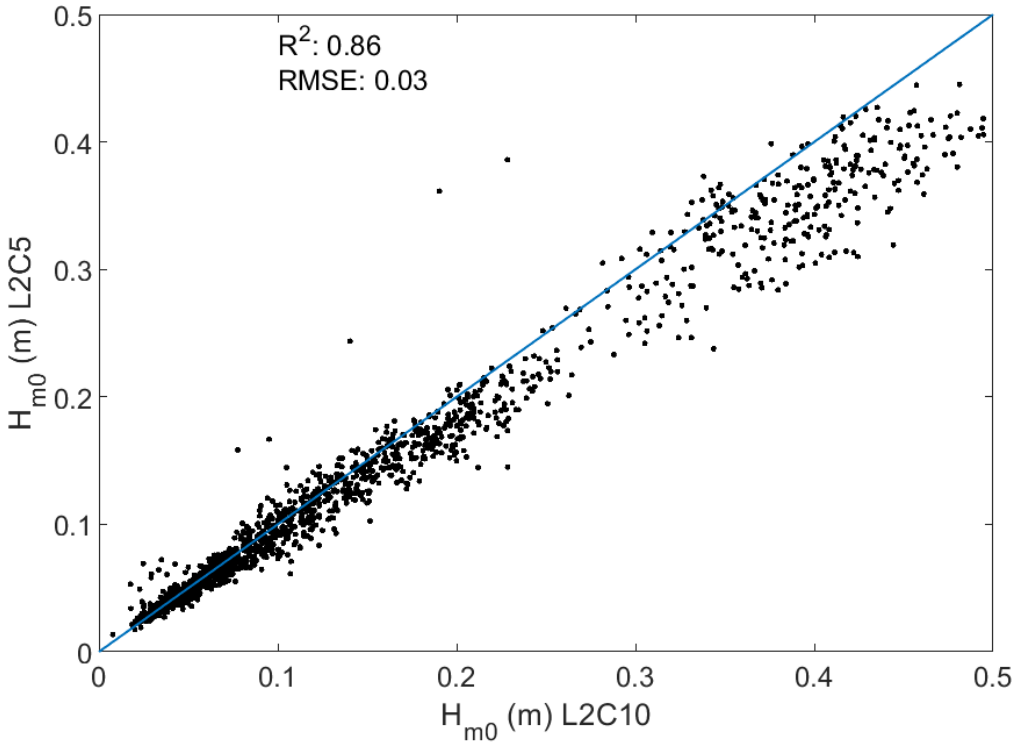

Figure 15: Significant wave height comparison between L2C5 (Keller pressure sensor) and L2C10 (OSSI Wave Gauge).

3.3.3 Sediment turbidity and transport

Several steps were taken to process the raw STM data. Firstly, the data needed to fulfill two requirements; The sensor height of the lowest sensor in the STM array had to be between 0.02 and 0.1 m above the bed, and the water depth above the sensor was at least 20 cm. An attempt was made to calibrate the sensors by using calibration curves for these specific instruments from previous field campaigns. However, the calibration resulted in a concentration profile that was highly variable over depth. The uncalibrated

data did have a clear Rouse profile. It was therefore chosen to continue with the uncalibrated turbidity data until new calibration curves are available.

During further processing the turbidity was averaged in blocks of 10 minutes. The 0.5^{th} percentile of the 10 minute turbidity signal was removed to correct for a background turbidity (De Bakker et al., 2016). Lastly the turbidity time series were checked for air bubbles. These are identified when the turbidity of higher sensors suddenly jump and are higher than the turbidity closer to the bed, these were manually removed.

The total turbidity in the water column (T) is calculated by linearly interpolating the measured turbidity's at the 7 different depths measured by the STM array and two individual STM's (T_{fitt}). This was subsequently integrated over water depth h:

$$T = \int_0^h T_{fitt}\ dz \tag{5}$$

Multiplying the concentration with the flow velocity yields the sediment transport rate (q_s):

$$q_s* = TU \tag{6}$$

In the future, a depth integrated velocity can be applied when the ADV's from location L2C5 are all processed.

The measured transport is compared to the suspended sediment transport formula of Van Rijn (2007*b*), which reads:

$$q_{s\ van\ Rijn} = 0.012\rho_s U D_{50} M_e^{2.4} (D^*)^{-0.6} \tag{7}$$

In which ρ_s is the sediment density, taken as 2650 kg m^{-3} and D_{50} the median grain size in m. $D*$ is the dimensionless particle size and M_e is the mobility parameter which were calculated by Equations 8 and 9:

$$D_* = D_{50}[(s-1)g/v^2]^{\frac{1}{3}} \tag{8}$$

In which s is the relative density of the sediment in the water, g is the gravitational acceleration taken as 9.81 m s^{-2} and v is the dynamic viscosity (10^{-6}).

$$M_e = \sqrt{\frac{(U - U_{cr})}{[(s-1)gD_{50}}} \tag{9}$$

This mobility parameter is dependent on the depth averaged critical velocity U_{cr} calculated as following:

$$U_{cr} = \sqrt{\rho_w \tau_{cw}} \tag{10}$$

In which ρ_w is the water density taken as 1025 kg/m^3. Calculation of the combined wave-current bed shear stress τ_{cw} will be elaborated on in Section 3.3.5. In order to compare the measured dimensionless sediment transport to the predicted data, the predicted data is also made dimensionless as done by Engelund and Fredsøe (1976).

$$q_{s* \ van \ Rijn \ (2007)} = \frac{q_{s \ van \ Rijn \ (2007)}}{[(s-1)gd^3]^{0.5}} \tag{11}$$

3.3.4 Sediment composition

All sediment samples were oven dried and mechanically sieved. For each sample between 100 - 200 g of dry sediment was used for sieving. For the sediment samples taken on 16 and 20 September a extensive sieve tower with 23 sieves was used (Fig. 16). The sieving results were analysed in order to reduce the sieve tower without losing too much accuracy, resulting in a sieve tower with 13 sieves. As recommended by Blott and Pye (2001), at least sieves for every round phi value were used. At smaller grain sizes more sieves at half or quarter phi intervals were added to maintain accuracy at smaller grain sizes. Figure 16 shows the relationship between the two sieve methods. It shows that for the D_{10} and D_{50} there is hardly any difference between the sieve towers. The largest difference for the D_{50} is not more than 0.05%. However, there is a small over prediction when using the semi-fine sieve tower for some of the D_{90} value.

	D_{10}	D_{50}	D_{90}	**Total**
R^2	0.9980	0.9991	0.9937	0.9977
RMSE (μm)	5	16	247	143
$\bar{x}$ (μm)	525	1640	6325	2830

Table 4: R^2, RMSE and mean grain size per D_{10}, D_{50} and D_{90}. This validates the use of the smaller sieve tower.

From the sieved sediment, traditional grain size distribution curves were made. These are used to find the different modes of the the sediment samples. The grain size distribution curves are also used for analysing the distribution of sediments over time per location.

The grain size distribution curves were further analysed using the Gradistat grain size distribution and statistics package from Blott and Pye (2001). The program calculates the mean, mode, sorting, skewness and other statistics such as D_{25}, D_{50} and D_{75}. This is done arithmetically and geometrically

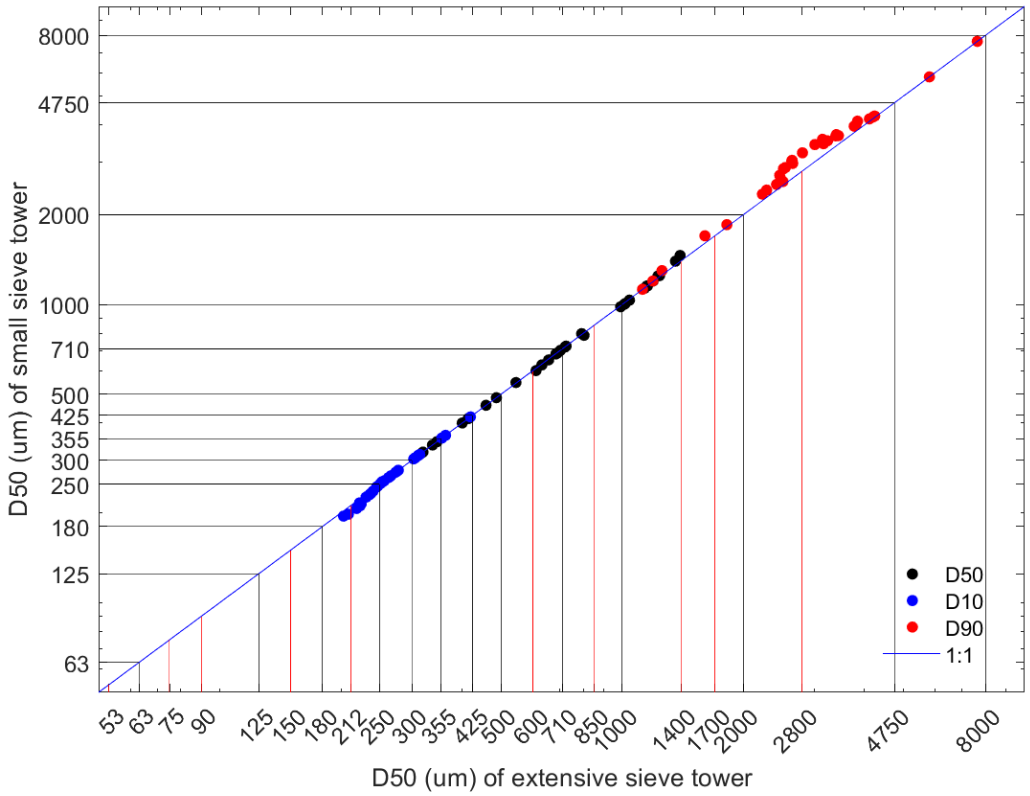

Figure 16: Validation to use a smaller sieve tower. The figure shows the relationship between the two sieve towers used. The vertical and horizontal lines indicate the sieve sizes of the extensive and small sieve towers respectively. Red vertical lines indicate removed sieves.

(in metric units) and logarithmically (in phi units) using moment the graphical methods from Folk and Ward (1957). The sediment sorting (σ_G) was mainly used in this study and was calculated as:

$$\sigma_G = exp(\frac{ln\ D_{16} - ln\ D_{84}}{4} + \frac{ln\ D_5 - ln\ D_{95}}{6.6}) \tag{12}$$

3.3.5 Sediment mobility

To identify the sediment suspension mechanisms, the time series of pressure and currents were used to calculate bed shear stresses (τ) in $\mathrm{N\,m^{-2}}$ and the dimensionless Shields number (θ). A hiding-exposure expression is added which all together indicates when sediment is theoretically mobilized. The Shields parameter is given by:

$$\theta = \frac{\tau}{(\rho_s - \rho_w)gD_{50}} \tag{13}$$

Where connotation of c and w at θ and τ represent the current and wave related θ and τ respectively. The D_{50} is time dependent and linearly interpolated from the 11 samples taken at different moments in time (Section 3.2.4). The wave-induced bed shear stress is calculated by following Soulsby and Clarke (2005):

$$\tau_w = \frac{1}{2}\rho_w f_w U_\delta^2 \tag{14}$$

In which U_δ is calculated using Equation 2. The wave friction coefficient f_w is calculated using the formulation of Soulsby (1997) which is dependent on the hydraulic regime:

$$f_w = \begin{cases} 2Re_w^{-0.5} & Re_w < 10^5 \quad laminar \\ 0.0521Re_w^{-0.187} & Re_w > 10^5 \quad smooth\ turbulent \\ 0.237r^{-0.52} & \quad rough\ turbulent \end{cases} \tag{15}$$

In this formula Re_w is the Reynolds wave number calculated by using the near bed orbital velocity and the orbital excursion length A_δ (Eq. 17).

$$Re_w = \frac{U_\delta A_\delta}{v} \tag{16}$$

$$A_\delta = \frac{Hm0}{2sinh(kh)} \tag{17}$$

The relative roughness (r) in Equation 15 is calculated by using the orbital excursion and the Nikuradse roughness (k_s) through:

$$r = \frac{A_\delta}{k_s} \tag{18}$$

In which the (k_s) is varying over time through the D_{50} and is calculated as:

$$k_s = 2.5 * D_{50} \tag{19}$$

The current related bed shear stress τ_c used to calculate the θ_c is determined after Soulsby and Clarke (2005):

$$\tau_c = \rho_w C_d U^2 \tag{20}$$

In which C_d is the drag coefficient (0.003) from Soulsby (1983). The combined bed shear stress from waves and currents is calculated using the the method of Grant and Madsen (1979) adopted by Zhu et al. (2016):

$$\tau_{cw} = \sqrt{(\tau_w + \tau_c\,|cos(\phi_{cw})|)^2 + (\tau_c\,|sin(\phi_{cw})|)^2} \tag{21}$$

In which ϕ_{cw} is the angle between the waves and currents in degrees.

The critical Shields parameter for incipient motion was calculated using the fitted Shields curve of Soulsby et al. (1997):

$$\theta_{cr} = \frac{0.24}{D_*} + 0.055[1 - exp(-0.020D_*)] \tag{22}$$

This equation does not include the increased critical Shields number for cohesive sediments. However, this is only relevant if the grain size is < 0.1 mm (Zuo et al., 2017), and was therefore found suitable for this study.

The θ_{cr} is valid when the sediment composition is homogeneous. In multimodal sediment mixtures the mobility of individual grains changes (Section 2.3.2). Currently, Equation 23 is often used to calculate the $\theta_{cr,i}$ in mixed beds (Wilcock and Crowe, 2003; Patel et al., 2013; McCarron et al., 2019).

$$\xi_i \equiv \frac{\theta_{cr,i}}{\theta_{cr,50}} = n\frac{d_i}{D_{50}}^{-y} \tag{23}$$

In which n = 1 for sediments with the same density. The value for γ in the expression is not easily determined. Several attempts have been made to formulate expressions for γ. Wilcock and Crowe (2003) expressed γ in terms of the bimodality index B. However, the correlation was found weak and it is only valid for bimodal sediment mixtures. Patel et al. (2013) expressed y in terms of sediment sorting. A recent study of McCarron et al. (2019) shows that the mobility was dependent on the percentage of coarse grains in the mixture. The γ-factor would increase when there are more coarse grains in the mixture.

Four gradations of hiding exposure are considered in this study by altering the γ exponent. This is done in order to analyse the sensitivity to the hiding-exposure effect. These are; When there is no hiding exposure (γ =1), and for $\gamma = 0.5$ and $\gamma = 0.75$. Furthermore γ is calculated by using the method of McCarron et al. (2019):

$$\gamma = \gamma_s + (\gamma_g - \gamma_s)f_g^{1.73} \tag{24}$$

In which γ_s is 0.68 and γ_g is 0.86 which were both empirically derived (McCarron et al., 2019). f_g is the fraction of gravel (2 – 64 mm) in the mixture obtained from Gradistat (Section 3.3.4), which is variable over time. This results in a γ fluctuating between 0.68 and 0.73.

The i^{th} grain size fraction is is in motion when $\theta_{cw,i} > \xi_i\theta_{cr,i}$. As the bed composition is known, Equation 13 can be rewritten in such a way that the grain size that exceeds the threshold of motion can be calculated over time

including varying bed composition and thus varying hiding exposure.

$$M_i = \frac{\tau}{\theta_{cr,i}(\rho_s - \rho_w)g} \tag{25}$$

This yields a mobility parameter M in m which is similar to that of Van Rijn (2007*b*). Yet, the mobility parameter of Van Rijn (2007*b*) used flow velocity and a critical flow velocity while rewriting Equation 13 uses the (critical) Shields parameter.

4 Results

4.1 Beach morphology

This section shows the temporal changes of the cross-shore profile, elevation changes at sensor locations and morphological developments. These are important to show when sediment has been transported.

Changes in bed elevation primarily occurred at the sloping part of the beach, between x = 15 and x = 45 m. Figure 18 illustrates the temporal changes in bed elevation. On September 13th, the beginning of the campaign, there was a constant sloping beach profile. Below the lower intertidal beach at x = 19 m, a steep beach step was present. Between 29 September and 2 October the profile flattened, where the upper part of the profile eroded while there was accretion at the lower part. The turning point is located at 0.3 m above NAP which is just above the MSL (0.14 m). The result is 20 - 40 cm of bed level change locally. Remarkable is the instantaneous way the profile changed between 30 September and 3 October (Fig. 18 a). In the next two weeks the profile slumped at the lower intertidal beach.

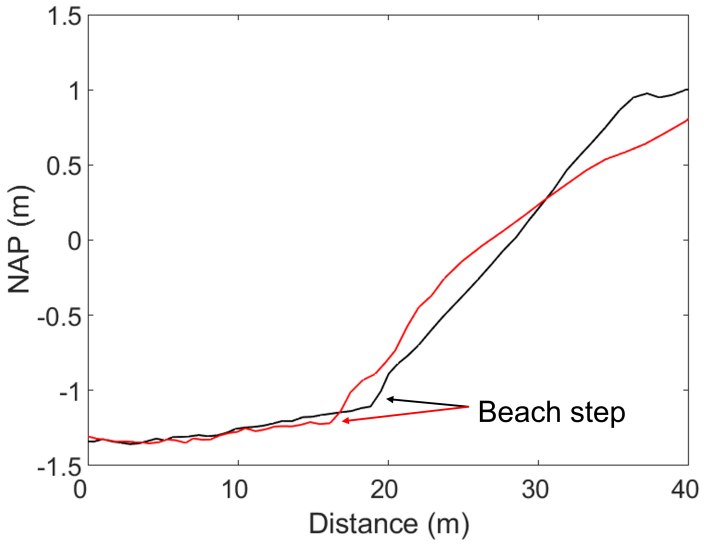

Figure 17: Profiles of 13 September (black) and 15 October (red) showing the distinct break in slope at the lower foreshore, indicating the presence of a beach step.

A beach step was present during the entire field campaign. However, due to the accretion in the lower intertidal beach the beach step moved 3 m seaward in October (Fig. 17). This is especially relevant considering the sediment sampling and STM sensors, this will further be discussed in

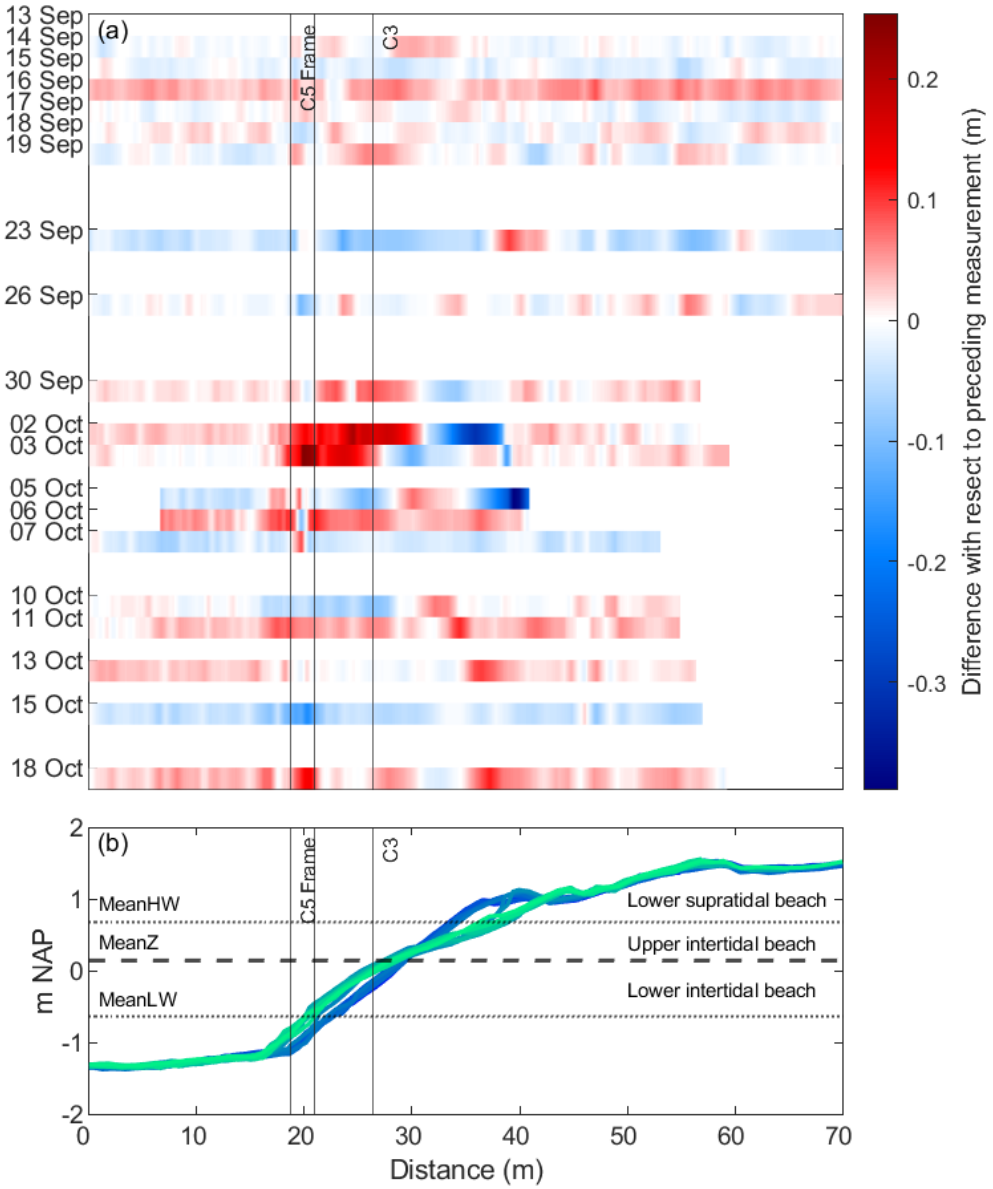

Figure 18: The temporal profile changes at L2. Top: changes in elevation with respect to the preceding measurement. Bottom: All measured profiles from 13 September (blue) to 18 October (light green).

the discussion. Furthermore, no berm was present at the beginning of the campaign (Fig. 18). However, the profile of 3 October shows that a berm developed on the lower supratidal beach at x = 40 m. This berm moved landward to x = 45 m and decreased in size over towards 6 October and remained static until the end of the campaign.

4.2 Sediment composition

The (change in) sediment composition is important when studying the mobility of sediments. This section aims to provide insight in the general properties of the sediment, the cross-shore variability and the temporal changes at two specific locations. These temporal variations will later be used to calculate the mobility over time.

4.2.1 General properties

Figure 19 shows the grain size distribution of all the sediment samples taken on the 20$^{\text{th}}$ of September (Tab. 3). The figure shows that there are three main sediment fractions visible in all samples. The most left peak represents a group with the finest grain sizes from 200 - 350 μm with the fraction 212 and 300 μm being most predominant. This is the fine to medium sand fraction. The next fraction is the coarse to very coarse sand fraction of 850 - 1180 μm. The coarsest group found in this sample set is the very fine gravel of 2 - 2.8 mm. From visual observations of the sediment samples and sieved fractions almost everything smaller than 710 μm consists of well rounded quartz grains. Everything which was larger than 710 μm was more mixed. This consisted of quartz grains, other minerals and significant amounts of shell fragments. Occasionally whole shells were found. During storm conditions between 30 September and 2 October a thick layer ($\approx$ 20 cm) of shells was found below the mean low water line.

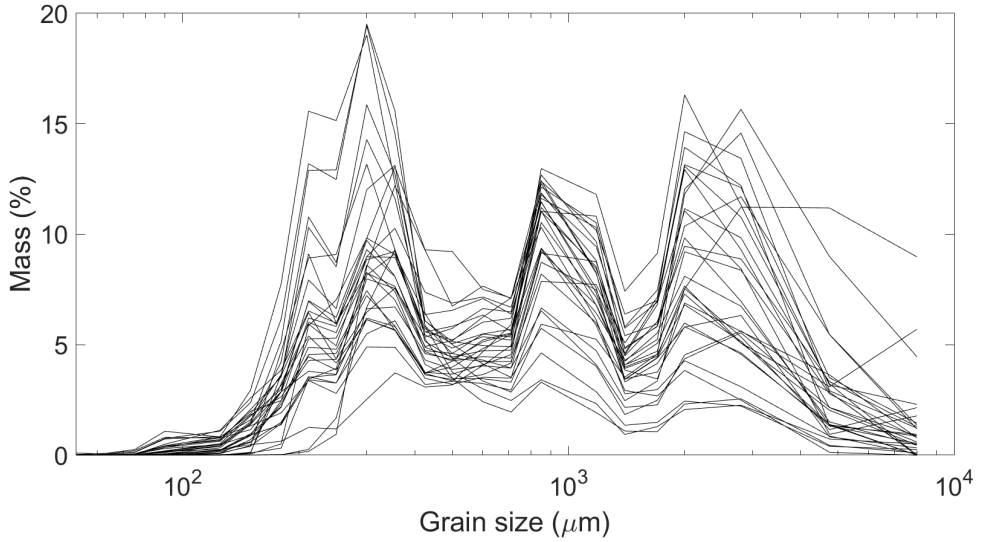

Figure 19: The grain size distribution of sediment samples taken on 20 September at L2

The sorting versus the D_{50} of the mixed sediment mixture at the foreshore and upper shoreface along L2 is shown in Figure 20. The figure shows the days where the entire cross-shore was sampled with the date in color and the location by marker type. In general the sediment at L2 is categorized as poorly sorted according to Blott and Pye (2001). A few samples are identified as moderately sorted and one as very poorly sorted. The variability in sorting is very high at 28 September while it is lowest at 15 October. Spatial variability of sorting is illustrated by the average sorting values per cross-shore location (Tab. 5). All values are very similar in range showing little spatial variability in how well a sediment is sorted.

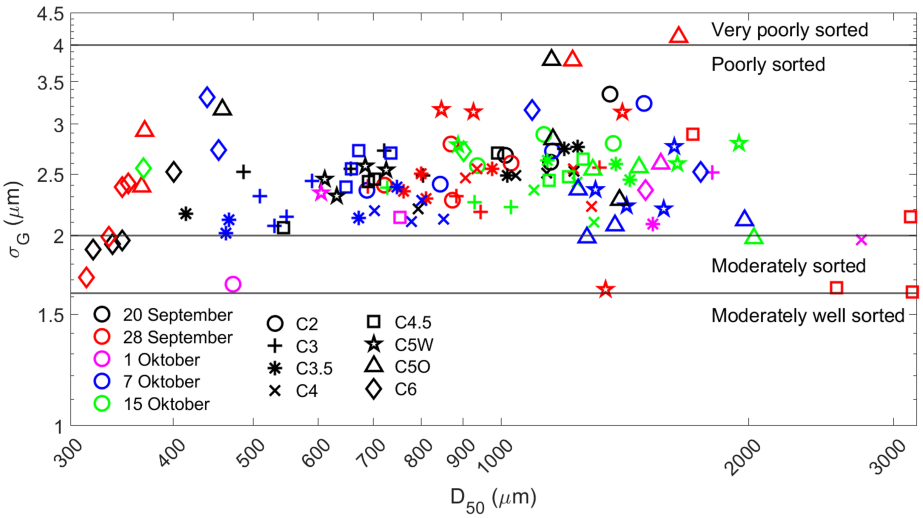

Figure 20: The D_{50} versus the sorting within each sediment sample (σ_G)

Location	**C2**	**C3**	**C3.5**	**C4**	**C4.5**	**C5W**	**C5O**	**C6**
Sorting	2.7	2.4	2.4	2.3	2.4	2.6	2.7	2.4

Table 5: The average sorting over L2, no significant difference in sorting is found.

4.2.2 Cross-shore variability in grain size

The cross-shore variability in total average grain sizes is shown in Figure 21a. It can be observed that the most landward sample taken at C2 is relatively coarse with a D_{50} of just above 1000 μm. At C3 the D_{50} is significantly lower with a value of 750 μm. From there the average D_{50} increases along the profile to 1300 μm at C4.5. It remains well above the 1000 μm at the

lower part of the steep slope at locations C5W and C5O. A little further seaward the average D_{50} strongly decreases after reaching the plateau at C6. The average D_{50} of all samples across the profile is 1032 μm. It can also be observed that the population standard deviation is the largest at the coarsest locations, in particular at L2C4.5. Where the population standard deviation at locations C2 to C4 is 200 - 300 μm it is 900 μm at C4.5. At C5 - C6 it is 400 to 500 μm.

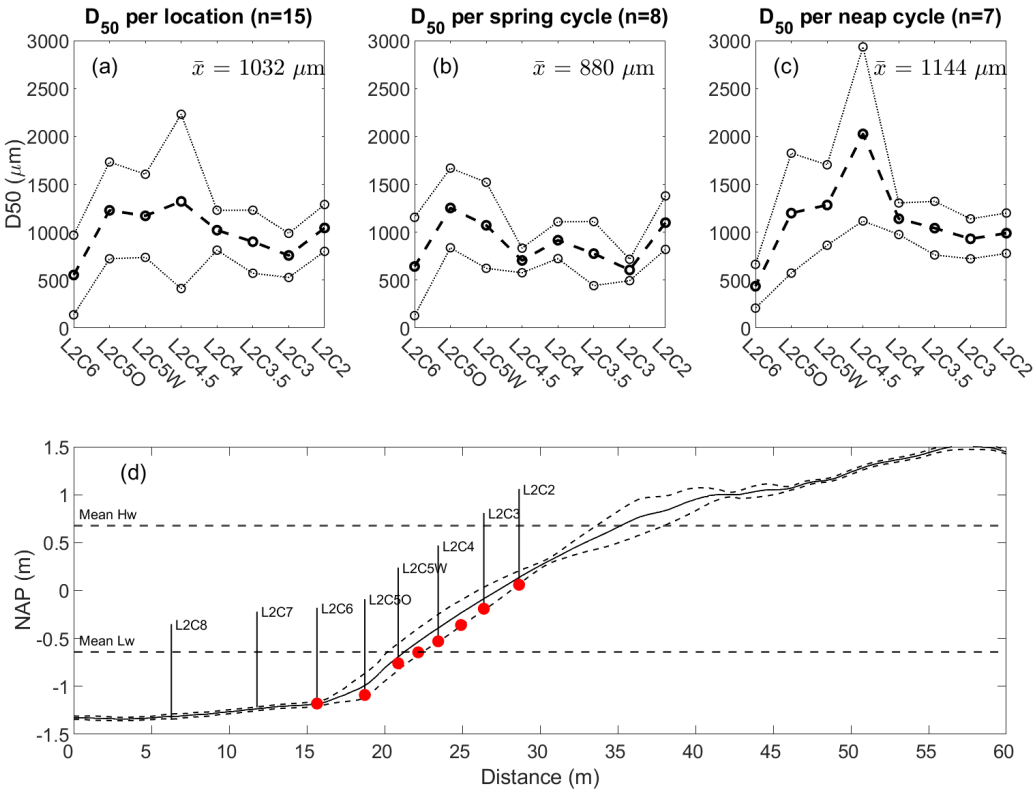

Figure 21: (a) The average D_{50} at each location at L2. A total of 15 samples per location. The average D_{50} at each location at L2 for the samples taken during spring tide (b), and during neap tide (c). The small dotted lines are the population standard deviations. The red dots indicating the cross-shore sediment sample locations (d).

The variations in grain size over the cross-shore profile during spring and neap tide is shown in Figure 21 b&c. The variability across the profile is similar when spring and neap are compared. The D_{50} at C2 is slightly coarser than that at C3, after which the D_{50} increases towards C5. The lowest D_{50} is found at C6. However, a main difference between spring and neap can be found at L2C4.5. During spring tide the D_{50} is lower than its surrounding

points with a very small standard deviation, which indicates little variation between the spring tide samples at C4.5. However, during neap tide the D_{50} at L2C4.5 is by far the largest of all locations, with also a very large standard deviation. Coarser grains are concentrated further up the slope during neap tide than during spring tide. This could indicate the movement of the beach step with the low water line (Section 5.1). In general the average D_{50} during spring tide was smaller (880 μm) than during neap tide (1144 μm).

4.2.3 Temporal variability of the sediment composition at L2C3

The temporal changes in particle sizes sampled during low tide at location L2C3 (Fig. 12 or 21d) is shown by plotting the grain size distributions over time (Fig. 22). Particle sizes smaller than 180 μm (mass % $\approx$ 0.5) and larger than 4750 μm (mass % $\approx$ 1.0) were rare. Furthermore, there is a distinction between particles smaller than 500 - 710 μm, which had less mass than particles larger than 500 - 710 μm. The first three samples taken at 16,

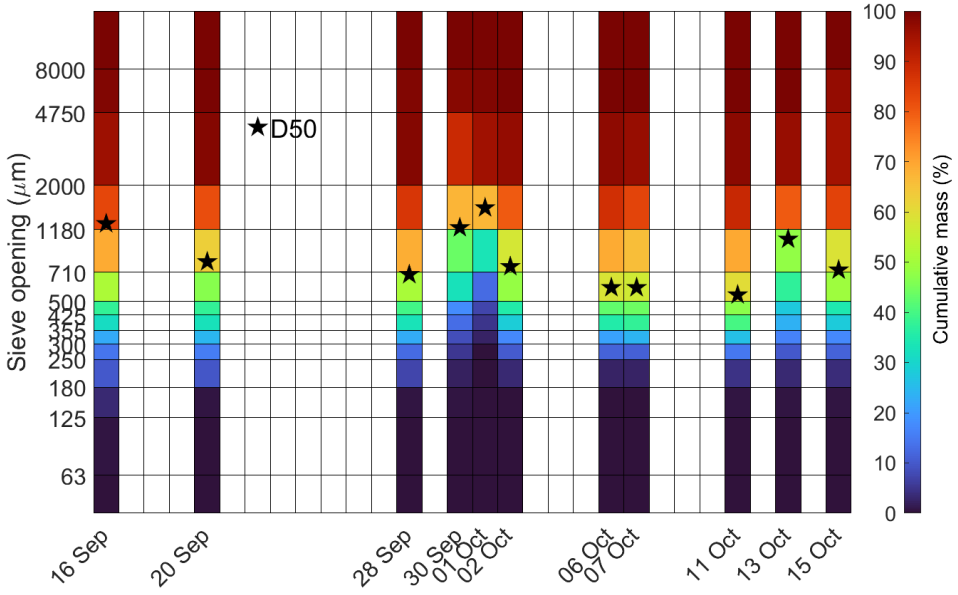

Figure 22: Grain size distribution over time for location L2C3.

20 and 28 September had a similar sediment composition, the finer sediment fraction between 180 - 710 μm became slightly more abundant towards 28 September. From 30 September to 2 October there was a significant change in the sediment composition, coinciding with an increase in coarser grains of 710 - 2000 μm and a decrease of the smaller grains for 30 September and 1 October. However, on 2 October, this coarsening of the bed has disappeared and the composition is similar again to samples prior of 30 September. After

this period the sediment remained finer (D_{50} = 540 – 590 μm) at 6,7 and 11 October with an increase in grains between 180 - 710 μm.

4.2.4 Temporal variability of the sediment composition at L2C5W

The temporal changes in grain sizes at location L2C5W is also shown (Fig. 23). Particle sizes smaller than 180 μm (mass % $\approx$ 0.2) were rare. Unlike C3, more particles larger than 4750 μm were present. Yet, the most mass % is still between 500 – 2000 μm.

At 16 and 20 September D_{50} was smaller at C5W (430 & 630 μm) than at C3 (1265 & 800 μm). Between those two days, the cumulative mass % of particles of 180 – 500 μm decreases (from 56 to 40 %) and increases for particles of 500 - 2000 μm (from 21 to 33 %). This continued up to 28 September, when there were little particles smaller than 500 μm. Between 30 September and 2 October the D_{50} decreases, and the composition changes as the abundance of grains of 710 - 4750 μm decreases while the abundance of grains of 180 - 500 μm increases. This change in composition was also observed at 6 and 7 October, where the D_{50} also decreases. Yet, from 28 September to 7 October the sediment composition was constantly relative coarse. At 11 October the D_{50} is relative small (864 μm). However, from 11 to 15 October the mass % of 1180 – 4750 μm particles increases (from 26 to 47 %), while everything below 1180 μm lost mass % (from 54 to 33 %), resulting in a increase in D_{50}.

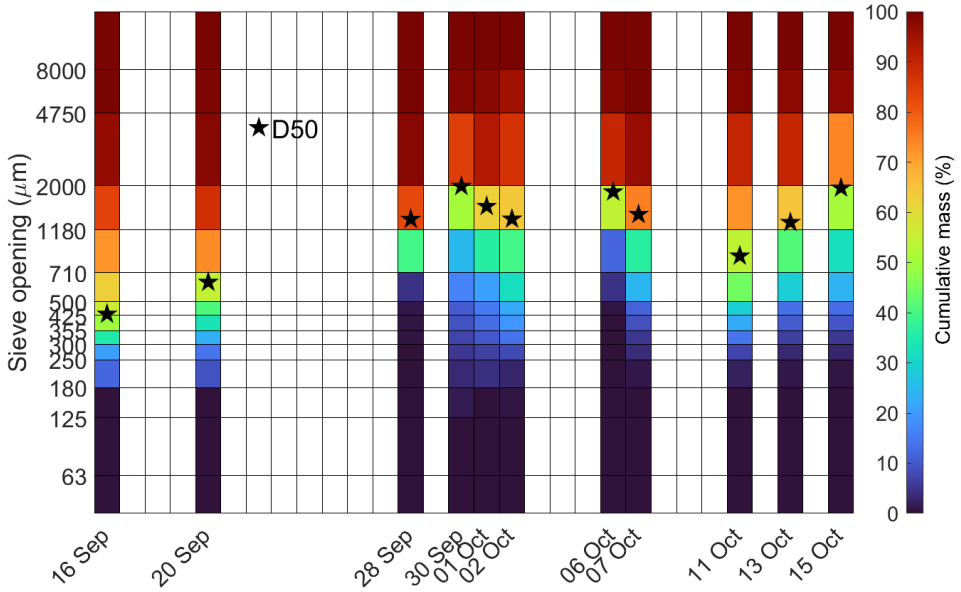

Figure 23: Grain size distribution over time for location L2C5.

4.3 Mobility and transport

To further analyse the conditions under which the different fractions were mobilized the wave and current-related Shields numbers ($\theta_{w,c}$) were calculated and compared to the turbidity (T). This is done to determine the relative importance of waves and currents. This is followed by an analysis of the calm (I) and storm (II) periods. Lastly, a more detailed analysis of the mobility of different grain size fractions over time was made.

4.3.1 Waves versus currents

To illustrate differences in sediment stirring and transport mechanisms turbidity and sediment flux are plotted as a function of θ_c and θ_w. Figure 24a indicates that the concentration is generally higher for a larger θ_w but it shows no clear differences in turbidity (T) for the θ_c. Furthermore, the threshold for incipient motion is far more frequently exceeded for θ_w. Figure 24b shows the same wave- and current-related θ but with the calculated sediment transport flux in color. This illustrates that transport fluxes are higher with larger θ_c, and thus with stronger currents.

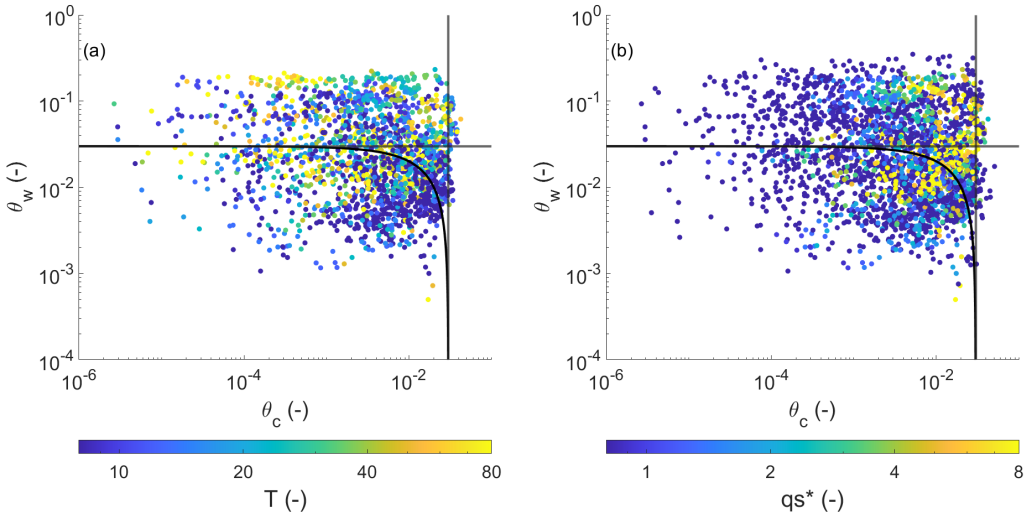

Figure 24: The wave- and current-related Shields numbers ($\theta_{w,c}$) for (a) Turbidity (T) and (b) sediment flux (q_s*). Horizontal and vertical black lines indicate the critical Shields number 0.03 (most occurring value from Equation 22) for both waves and currents. The curved black line is the combined wave-current critical Shields ($\theta_{cr,cw}$).

An overview of percentages time that grain sizes are possibly entrained is shown in Table 6. It shows the contribution of currents only, waves only

and the combined effect of waves and currents for different scenarios explained later in this Section. Generally it can be observed that, regardless the scenario, waves have more entrainment potential than currents and the combined effect is even larger.

4.3.2 Calm and storm period

The 10 minute averaged time series of T and θ is shown in Figure 25. T shows no clear relationship with any of the θ as peaks in T did not necessarily coincide with larger values for θ. The θ_w is on average approximately 5 times bigger than the θ_c. Within this time series three periods are identified. (I) Shows a period at the beginning of the campaign with relatively calm conditions with small and a relatively constant θ. (II) Is the period during the campaign which was most energetic and where the highest waves were measured, referred to as the storm period. (III) This period lies within the storm period but distinguishes itself by the remarkable low T measured in energetic conditions resulting in high θ values. Furthermore the currents have more stirring potential during the calm conditions (I) than during storm conditions (II), however they are very overall very low. For waves the stirring potential is much higher during the storm conditions (II).

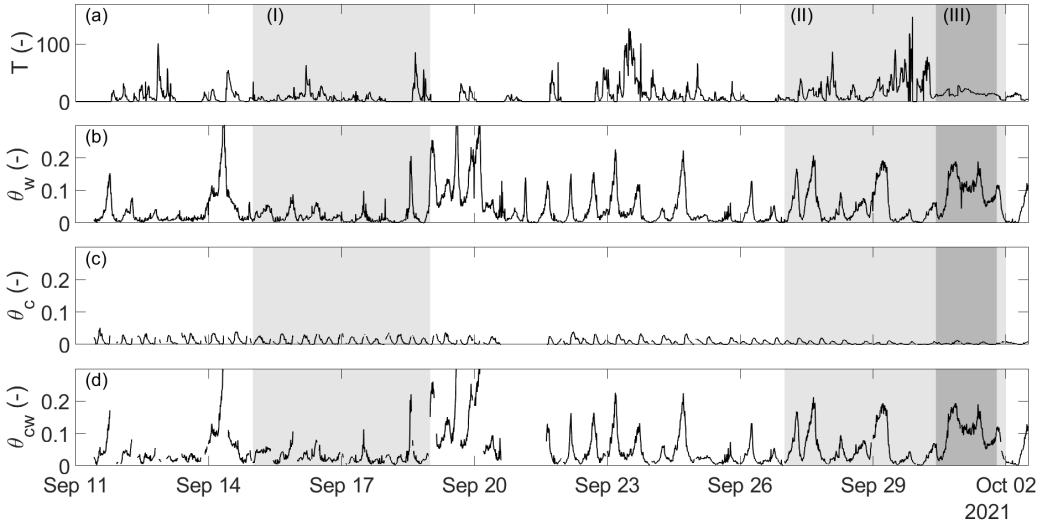

Figure 25: The temporal variability of (a) the total turbidity (T) over the entire depth measured at L2C5, (b) the wave-related Shields number (θ_w), (c) the current-related Shields number (θ_c) and (d) the combined wave-current-related Shields number (θ_{cw}). The grey shadings indicate (I) calm conditions, (II) energetic storm conditions, (III) significant reduction in measured turbidity during the storm period.

Figure 26 shows the turbidity, sediment mobility and Shields numbers during the calm period (I). During this calm period, there were a few moments where there were peaks in T, indicated by the red areas. Peaks 2 – 8 were all simultaneously with a reduction in θ_c and thus a slowing down of the current during either high or low tide. For peaks 4 – 7 the T was also high in when there was very little θ_c at slack water. Peaks 3,4,7 & 8 are the largest peaks in T. Those peaks also matched with periods where the mobility of D_{50} exceeds its threshold. For peaks 4 & 7 this was also after some peaks in θ_w. However, a increase in any of the θ or mobility is a guarantee in an increase in t. It is therefore clear that none of the parameters always matches the turbidity.

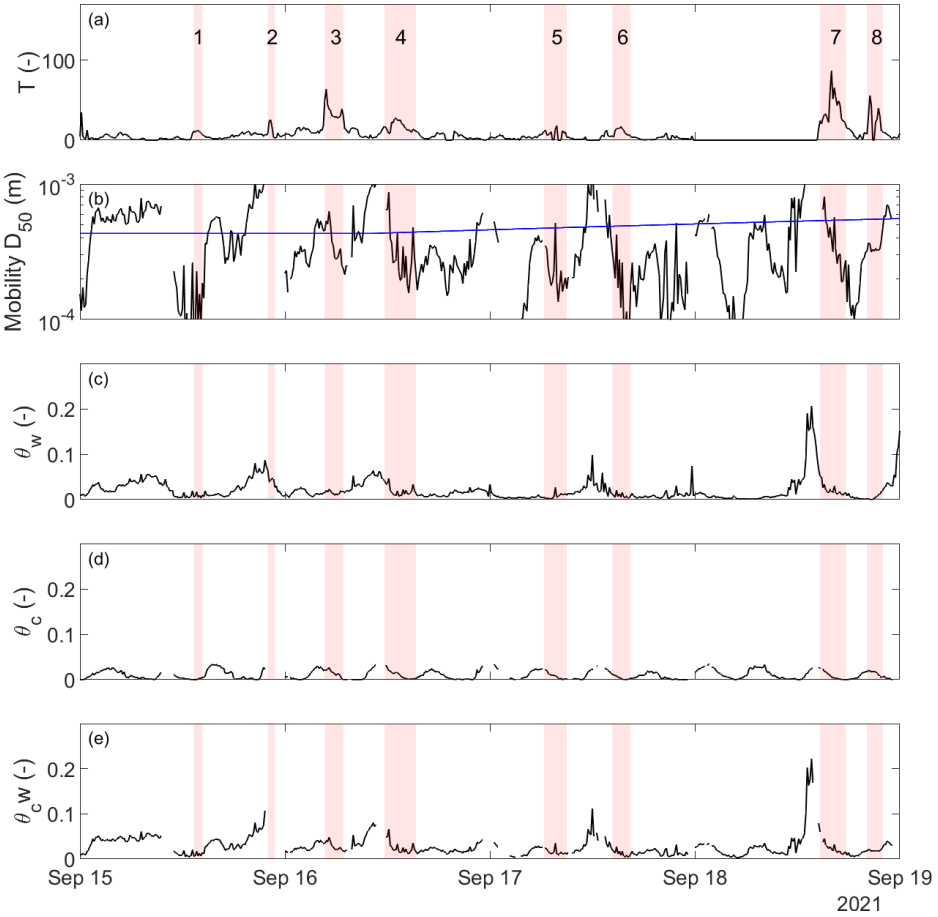

Figure 26: Time series of 10 minutes averages during calm conditions (I) for (a) turbidity, (b) sediment mobility, (c) waver-related shields, (d) current-related Shields and (e) the combined wave- current-related Shields. The red areas indicate moments of turbidity peaks. The y-limits are the same as Figure 27 for convenient comparison.

Figure 27 also shows the T, mobility of the D_{50} and θ. T peaks 2 and 5 occurred simultaneously with peaks in the mobility and θ_w. T peak 1 occurred during maximum θ_c just after a peak in mobility and θ_w. Peaks 3 % 4 do not relate to any of the parameters. T peaks 6 & 7 occur simultaneously with peaks in the θ_c & θ_w. However, the peak in θ is relatively small while the measured turbidity is relatively high. During period (III) the mobility almost always exceeds the threshold and the θ_w is very high, yet the measured T remains relatively small, suggesting a reduction in mobility or availability.

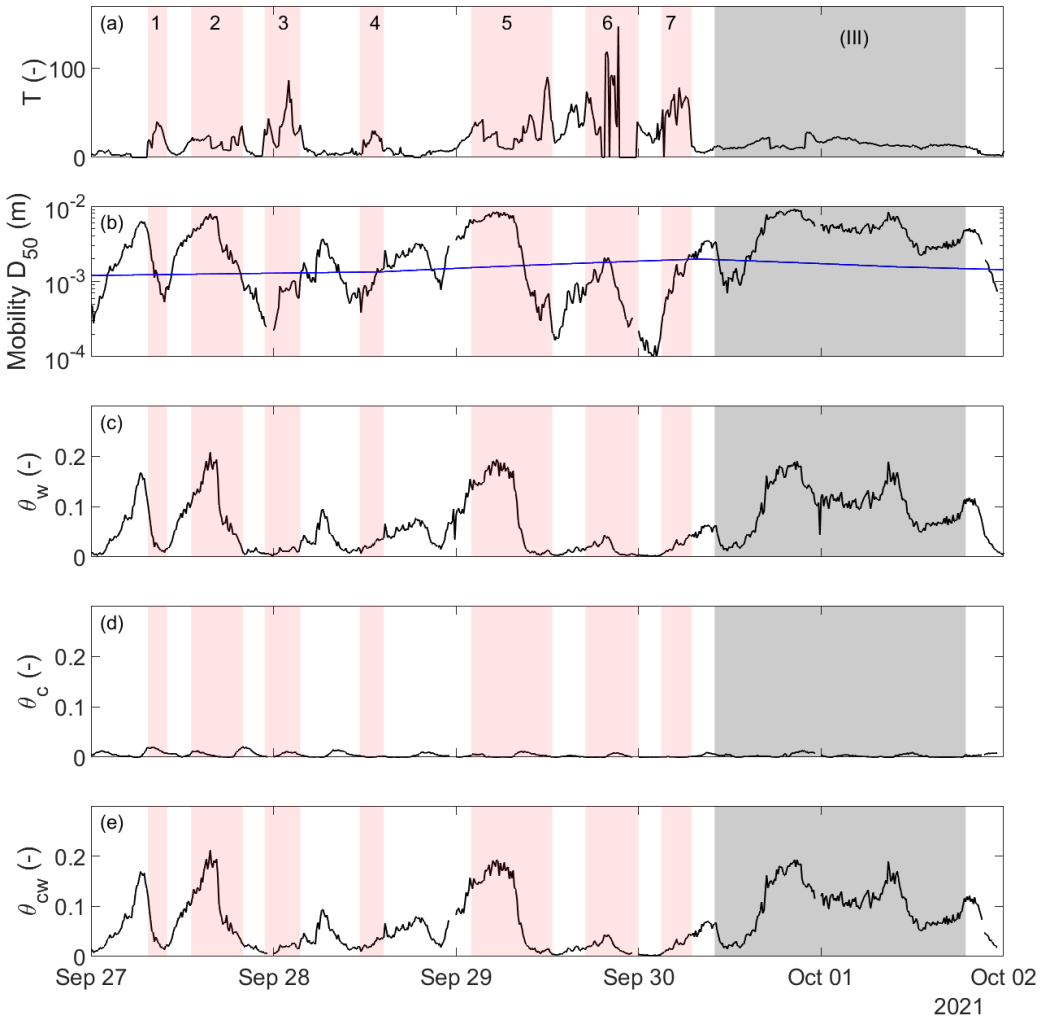

Figure 27: Time series of 10 minute averages during storm conditions (II) for (a) turbidity, (b) sediment mobility, (c) waver-related shields, (d) current-related Shields and (e) the combined wave- current-related Shields. The red areas indicate moments of turbidity peaks. The y-limits are the same as Figure 26 for convenient comparison.

	Currents only				Waves only				Combined			
	No HE	**HE γ=0.5**	**HE γ=0.75**	**HE Fg***	**No HE**	**HE γ=0.5**	**HE γ=0.75**	**HE Fg***	**No HE**	**HE γ=0.5**	**HE γ=0.75**	**HE Fg***
					ENTIRE PERIOD							
D_{10}	11.1	2.7	1.3	1.6	52.6	44.6	40.1	41.2	59.4	48.4	42.3	43.5
D_{50}	1.8	1.8	1.8	1.8	39.4	39.4	39.4	39.4	41.7	41.7	41.7	41.7
D_{90}	0.0	0.0	0.0	0.0	7.1	17.0	23.5	22.1	7.2	16.4	23.3	21.4
					CALM							
D_{10}	11.4	0.9	0.2	0.5	27.4	17.7	14.0	15.4	41.4	27.4	19.9	21.8
D_{50}	1.2	1.2	1.2	1.2	19.6	19.6	19.6	19.6	28.6	28.6	28.6	28.6
D_{90}	0.0	0.0	0.0	0.0	0.2	1.7	3.1	2.8	0.3	1.6	3.5	2.4
					STORM							
D_{10}	5.3	0.0	0.0	0.0	79.3	71.6	67.0	67.7	85.2	75.3	69.3	70.0
D_{50}	0.0	0.0	0.0	0.0	58.3	58.3	58.3	58.3	60.2	60.2	60.2	60.2
D_{90}	0.0	0.0	0.0	0.0	15.5	34.0	41.5	39.9	16.1	34.3	42.9	40.1

Table 6: Percentage of time the sediment size (D_{10},D_{50} & D_{90}) are possibly entrained considering currents only, waves only and the combined effect. The percentage is calculated without using a Hiding-Exposure (HE) effect and with a constant γ (0.5 & 0.75) and a time variable γ dependent on the fraction of gravel, Fg* (see method). It varies between $\gamma = 0.68$ and $\gamma = 0.73$.

4.3.3 Considering multiple grain size fractions

The mobility of the different sediment fractions at L2C5W is calculated by using the interpolated grain size and hydrodynamic conditions (Eq. 25). This is illustrated in a time series shown in Figure 28, which shows the sediment size that theoretically can be mobilized for no hiding-exposure (a) and with the hiding-exposure expression and γ exponent (Eq. 23 & 24) for the D_{10}, D_{50} & D_{90} (b,c & d). Table 6 shows the percentage of time the different fractions are possibly mobilized for the entire period, the calm period (I) and the storm period (II). Different hiding-exposure factors are considered as explained in Section 3.3.5.

When no hiding-exposure is considered (Fig. 28a) only the D_{10} & D_{50} fractions were possibly entrained during the calmer period (I). The mobility line only exceeds the grain sizes of both D_{10} & D_{50} fractions (41.4 & 28.6 % respectively). During the storm period, all fractions are sometimes theoretically mobilized. The D_{10} fraction most often exceeds the mobility (85.2 %), than the D_{50} fraction (60.2 %) and the D_{90} fraction the least often (16.1 %).

The mobility of the D_{10} fraction decreases significantly (from 59.4 to 43.5 % over the entire period) if the hiding-exposure factor of McCarron et al. (2019) (Fg*) is taken into account (Fig. 28 b). This decrease is even larger during the calm period (from 41.4 to 21.8 %) while it is less during the storm period (from 85.2 to 70.0 %). The mobility of the D_{50} never changes using this hiding-exposure function as the fraction D_i/D_{50} is always 1. The mobility of the D_{90} fraction increases significantly with the hiding-exposure factor (Fg*) incorporated (from 7.2 to 21.4 % over the entire period). The D_{90} fraction is 8 times more time mobilized during the calm period, yet it remains a small amount of the time (from 0.3 to 2.4 %). During storm conditions the time the D_{90} fraction is mobilized increases from 16.1 to 40.1 %.

Another factor which influences the mobility, and was taken account of, is the grain sizes present in the bed. There was a larger portion of small sediments available during the calm period (Section 4.2.4) which contributes to the D_{10} being possibly entrained. Therefore the presence and availability of sediments is important during this period. Furthermore, there was a coarsening in the bed during moderate conditions between 19 - 27 September. During this period the D_{10} and D_{50} are possibly entrained during significant amounts of time. However, during the storm period the bed has a wider distribution (the D_{10} in Fig. 28b goes down and the D_{90} in Fig. 28d goes up) causing even larger differentiation between sediment sizes which are possibly entrained.

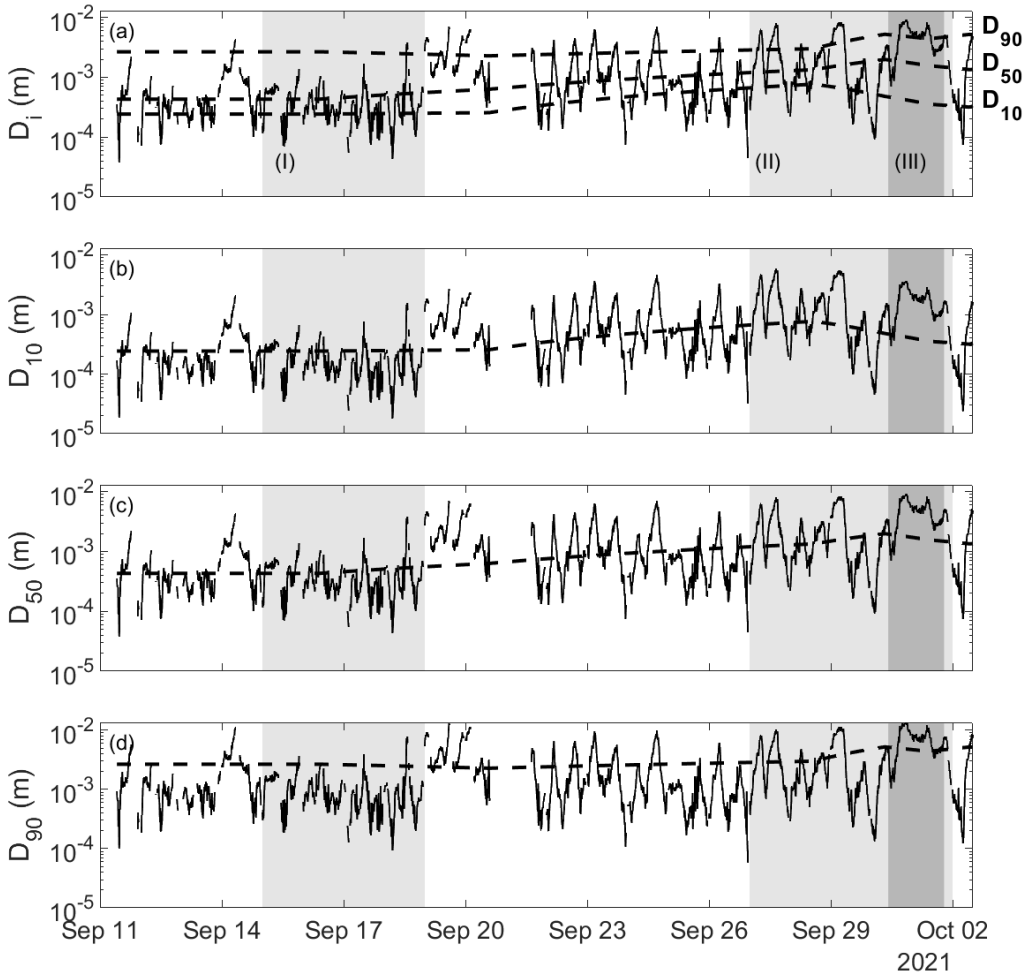

Figure 28: The sediment size that is in motion for (a) no hiding-exposure (b) the D_{10} fraction with hiding-exposure, (c) the D_{50} fraction with hiding-exposure and (d) the D_{90} fraction with hiding exposure. Dashed lines indicate the measured grain size of the respective D_i. The grey shadings indicate (I) calm conditions, (II) energetic storm conditions, (III) significant reduction in measured concentration during the storm period.

4.4 Comparison with prediction

A comparison between measured and predicted suspended sediment transport is made (Fig. 29). Due to the fact that the measured data is not calibrated the numbers could not be compared directly. Therefore the (dimensionless) predicted sediment transport ($q_{s* \textit{ van Rijn}\ (2007)}$ & $q_{s \textit{ van Rijn}\ (2007)}$) was compared to the dimensionless measured transport ($q_{s \textit{ measured}}$). Especially the different identified time periods can compare to each other. In a

general sense, the calm period (I) results in the lowest measured transport and the storm (II) in the highest measured transport rate while the period (III) is in between. The largest scatter is during the calm period while period (III) has the least scatter for both the measured and predicted transport rates (Tab. 7). Period (III) shows the largest over prediction for the predicted sediment transport while this is not the case for the dimensionless sediment transport due to the relative coarse grain size. The measured data has more scatter than the predicted data.

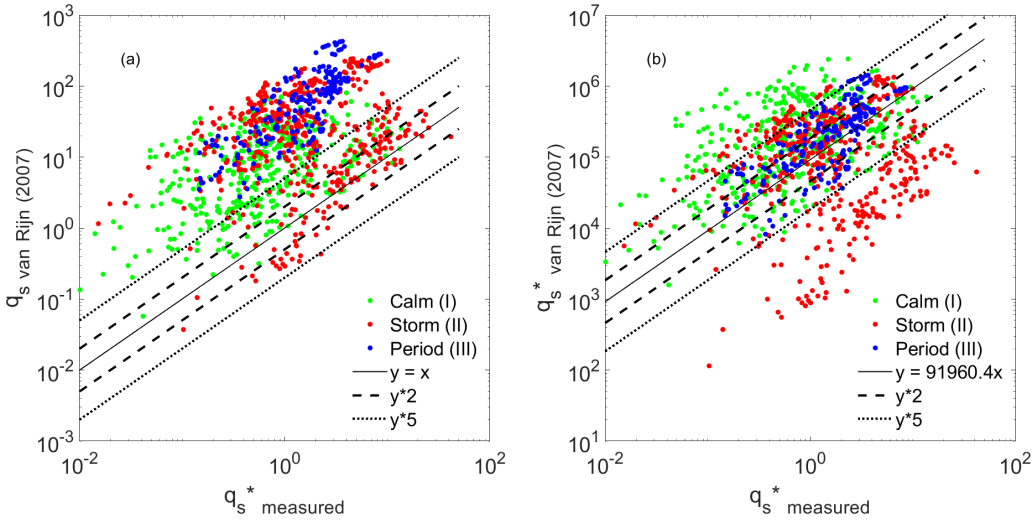

Figure 29: Predicted versus measured dimensionless sediment transport for (a) van Rijn (2007) and (b) dimensionless van Rijn (2007). The black line indicates a linear fit and dashed and dotted lines indicate the 2 or 5 times the linear fit respectively.

	Measured			**van Rijn 2007**			**van Rijn 2007***		
	$\bar{x}$	**std**	**% std**	$\bar{x}$	**std**	**% std**	$\bar{x}$	**std**	**% std**
All	1.8	3.4	189	19	26.4	139	410220	714611	174
(I)	1.0	1.9	190	9.5	13.0	137	347183	522693	151
(II)	2.6	3.7	142	26.7	32.2	121	240899	296991	123
(III)	2.0	1.6	80	41.4	43.0	104	326119	325370	100

Table 7: Summary of the mean, standard deviations and percentage the standard deviation is from the mean for the dimensionless measured and predicted values per time period.

5 Discussion

In this section, the cross-shore sediment composition and morphology will be discussed and put into a conceptual Figure for beach states. Thereafter, the impact of the complex sediment mixture on the mobility will follow. Factors and processes discussed are preferential transport, hiding-exposure, armouring and sediment mixing. A conceptual model for morphological development and sediment mobility is presented in light of all aforementioned concepts. Next the prediction of sediment transport is discussed. The section will end with the limitations of this study and recommendations for future research.

5.1 Cross-shore sediment composition & morphology

Observations on grain sizes and the morphology are used to identify different observed beach states. The sediments found at location L2 show three grain size modi; 250 μm, 850 μm and 2500 μm (Fig. 19). The 250 and 2500 μm coincide with the smallest and largest grain size used during construction according to Jan de Nul (Tab. 1). However, Jan de Nul reported grain sizes with a D_{50} larger than 400 μm, rather than D_{50} equals 400 μm. This is a relative unclear grain size which in this study seems to relate to grain size modus of 850 μm. However, this is well plausible as Jan de Nul used a very small sieve tower for the sediment analysis which could result in less precision in the grain size modi. The data suggests that the sediment composition was coarser during neap tide (Fig. 21). However, it is likely that this is largely influenced by storm conditions on 28 September and coarsening due to preferential transport (Section 5.2.1) prior to 15 October. Shell fragments were observed throughout the entire cross-shore profile (Section 4.2.1) and were responsible for a part of the large grains. However, this study did not identify how much shell fragments were present or distinguish the shells from grains in any way. Furthermore, the influence of shells on sediment transport was not taken into account.

The mixed sediments are poorly sorted ($\sigma_G = 2.3 - 2.7$) across the entire cross-shore profile (Fig. 20, Tab. 5). This emphasizes the fact that sediment entrainment and transport over the beach face is strongly influenced by the complex mixtures (Section 5.2.1). The observed fining trend in offshore direction (Fig. 21) corresponds to findings in other studies (Guillén and Hoekstra, 1996; Reniers et al., 2013; Huisman et al., 2016) at different types of beaches, which could imply less energetic conditions in offshore direction.

At location L2, the coarse sediment at the shore break was identified as a beach step (Fig. 17). It was visually observed that the beach step was consistently moving up and down the beach. Coarser sediment was

found higher up the beach during neap tide than during spring tide (Fig. 20), indicating that the beach step moves with the mean low water. This is consistent with visual observations and the findings of a pure gravel beach in a macrotidal environment of Austin and Buscombe (2008). The presence of the beach step at the lower fore shore could possibly result in large differentiation in grain size over a short distance due to sediment sampling at the beach step or just next to it. Sediment samples collected at location L2C5 are in close proximity of the beach step. Furthermore, it could be important location for mixing the bed (Section 5.2.4).

The relative steep beach profiles (Section 2.1) and coarse grains shows resemblance with the classification system of Jennings and Shulmeister (2002). However, there is not one of the beach types that fits perfectly. The intertidal zone at L2 looks like the mixed sand gravel beach type due to the sediment composition, occasional berm development and the mean low and high water levels which are located on the steep part of the beach. Due to the fact that the PHZD is an artificial structure build on a shallow shoal, the sand dominated offshore part of a composite gravel beach is also present. However, a difference is that the low water line of a composite beach is located at this sandy part. However, some shoaling of waves (Fig. 15) occurs at L2, which is typical for the composite gravel beach, implying that this location has characteristics of both an mixed sand gravel and a composite gravel beach.

5.1.1 Conceptual beach states

Apart from these classification types there were also two conceptual beach states identified at L2, which are shown in Figure 30. During the calm conditions (period I) there was a relative steep beach, and over time the sediment also got coarser (Section 4.2.4). Beneath the coarser grains the finer sediments were located as also shown in the picture in Figure 30. After the storm period (II) the beach profile was flatter and the sediment composition was finer (11 Oct, Fig. 23). However, the picture in Figure 30 shows that below the fine sediments a more mixed and coarse layer was present. These two beach states are important because sediment transport must have taken place, indicating that sediment must have been mobilized.

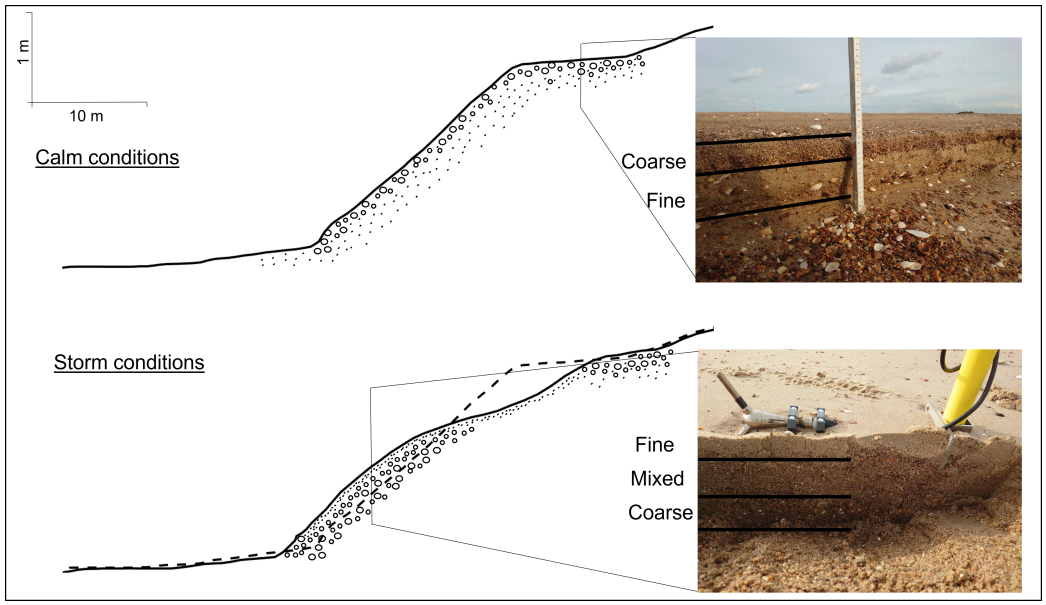

Figure 30: Conceptual figure of beach states

5.2 Temporal variability in sediment composition and mobility

It is well known that temporal variability in sediment composition can be linked to changes in hydrodynamics (Slingerland and Smith, 1986). In this Section the effect of waves and tides on the preferential transport of finer sediments is discussed, which can affect the sediment composition. Afterwards, the effect of hiding-exposure, armouring and sediment mixing on preferential transport is discussed. At last, dominant processes affecting the mobility will be combined with the beach states to form a conceptual model.

5.2.1 Preferential transport

There are several results from this study that point towards possible preferential transport at the PHZD. The Shields number is often around the temporally varying threshold for incipient motion, which could imply differentiated mobilization (Huisman et al., 2016). Or as illustrated in Figure 28, smaller grains are mobilized more frequently than coarser grains. This is further supported when we observe the percentage of time different fractions are possibly in motion. Where the D_{10} has the possibility to be in motion 27 - 47.9 % of the time, while this is only 26 % for the D_{50} and 0.2 - 9.9 % for the D_{90} (Tab. 6). Even though the conditions are considered mixed, the waves are the dominant factor in mobilizing sediments (Fig. 24, Tab. 6)

while the currents are important for sediment transport (Fig. 24).

The coarsening of the sediment composition from 16 September towards 28 September further supports the hypothesis of preferential sediment transport, as also observed by Huisman et al. (2016), because the sediment mixture becomes coarser when smaller grains are transported. From the beginning of the campaign until prior to the storm conditions, approximately 5 cm was eroded at the location of the frame (Fig. 18). Considering the dominant transport direction at L2 is towards the North (Woerdman, 2022), it would be expected that sediments deposited at the northern part of the spit have a relatively smaller D_{50}. Sediment samples taken at the most extended part of the spit is indeed show a relative small D_{50} of 350 - 650 μm (Woerdman, 2022).

During calm conditions the D_{90} is only mobilized for 0.3 to 3.5 % of the time while the D_{10} is mobilized 19.9 to 27.4 % of the time. Depending on the degree of hiding-exposure (Section 3.3.5) preferential transport can prevail during calm conditions. During storm conditions larger grains are also possibly mobilized (Fig. 28). Therefore preferential transport during storm conditions is limited, but there was more sediment mixing as more fractions are in motion (Tab. 6 & Section 5.2.4). This is consistent with the findings of Huisman et al. (2016). However, Figure 28 suggests that during the moderate conditions between the calm and storm conditions also has potential for preferential transport as the D_{10} is exceeding the threshold for incipient motion more often than the D_{90}.

5.2.2 Hiding-exposure

The poorly sorted sediment (Fig. 20) suggests that hiding-exposure effects were almost always relevant at L2. However, Figures 22 & 23 show that during the calmer conditions at the beginning of the campaign and after the storm conditions the sediment has a wider distribution, resulting in better hiding of small grains and more exposure of larger grains as derived from Equation 23, which reduces the effect of preferential transport.

Furthermore, the results of this study show that the mixture is very variable over time. This complicates incorporating the hiding-exposure effect in models. The time varying γ from McCarron et al. (2019) could be a solution for this. The calculated gravel fraction dependent γ of McCarron et al. (2019) varies between 0.68 and 0.73 only (Section 3.3.5). This is within the range of values of McCarron et al. (2019), who found values from 0.68 (pure sand) to 0.86 (pure gravel). Therefore the range found for this location could be considered small. The percentage of time the Shields number exceeds the threshold for incipient motion for $\gamma = 0.75$ is very similar to the varying

γ of McCarron et al. (2019). As the range is thus relatively small and the effect on incipient motion is limited, a constant γ factor (for instance ≈ 0.7) could also be appropriate for this location in case no time series of sediment samples are available.

5.2.3 Armouring

During the storm period there were several periods during which a high turbidity was observed (Fig. 27). However, one period (III) near the end of the data shows significantly lower turbidity. This period lasts from 30 September to 2 October. The reduced measured turbidity are not a result of the sensor being buried for two reasons: 1) RTK-GPS measurements show that deposition at this location only took place after this event (Fig. 18). 2) The reduced turbidity was observed at all five sensor in the water column. Visual observations from 29 September indicate that there was a very thick (20 cm) layer of shells around the low water line. It is very likely that this was around the location where the OBS sensors were deployed, resulting in significant armouring as observed by Miedema and Ramsdell (2011) and Diedericks et al. (2018). When the predicted dimensionless sediment transport was compared to the measured dimensionless transport (Fig. 29), the largest relative over prediction of the sediment transport was during this shell armoured period, indicating that a larger sediment transport would indeed be expected during this period. The observed grain size at location L2C3 was much smaller on 2 October ($D_{50} = 760$). Combined with the fact that the largest morphological changes were also observed during this same period (Fig. 18), this illustrates that the large accumulation of shells only limited transport very locally. It is unclear when or how this armour layer developed.

In the period prior to the storm preferential transport prevailed (Section 5.2.1). This indicates that apart from hiding effects, no armoured layer was fully developed yet. However, during this period the armoured layer could develop due to the removal of fine sediments by preferential transport, leaving only coarser sediments behind. Figure 25 shows no noticeable reduction in sediment turbidity prior to the storm period. There are two possible reasons for this: 1) It could be that exposure effects increase the mobility of larger fractions so drastically that the effect of armouring is negligible. However, this is considered unlikely due to the observed coarsening of the bed (Fig. 23), which implies coarser fractions were still relatively immobile compared with finer fractions which is substantiated by the low amount of time D_{90} is theoretically mobilized (Tab. 6). Or 2) it could imply that a coarse enough bed layer to act as armour layer was underdeveloped and would take longer to form. There are recent developments in studies identifying the dimensionless

equilibrium time at which an armoured layer has formed (Berni et al., 2018). If an armour layer develops fast, it could reduce sediment transport for a longer period. This is especially relevant compared to how often the sediment gets mixed (Section 5.2.4) and will be further discussed within the framework of the conceptual model. Current studies on the equilibrium time such as Berni et al. (2018) were only under steady flow in laboratory conditions. Further verification in unsteady field conditions would be an interesting topic for future research.

5.2.4 Sediment mixing

The results from the multi-fraction mobility analysis (Section 4.3.3) show that all fractions can be mobilized during higher waves (period II) which corresponds to the findings of Huisman et al. (2016) at the Sand Engine and implies that waves are responsible for the extensive mixing. This is further substantiated by the fact that waves showed higher θ values than currents (Fig. 24). However, the conditions between Sand Engine and the PHZD are different. The storm conditions considered in this study were wave heights that would be considered calm conditions at the Sand Engine (≈ 0.5 m). This rises the question why these relative small waves can cause such significant sediment mixing. This is likely related to the mixing depth, which not only increases with significant wave height (Gómez-Pujol et al., 2011), but also with steeper slopes (Ferreira et al., 2000), increasing the mixing capacity. The naturally steep slopes of gravel beaches (Section 2.1) is thus also increasing the mixing capacity, mainly due to the presence of the beach step which is the most energetic zone. As the beach step moves up and down the beach with the tidal cycle (Section 2.1) this could result in mixing of the large parts of the bed.

The mixing of sediment is important because it increases the availability of fine sediments which counters the armouring effect and increases preferential transport. In contrast to the Sand Engine, where it is expected that all the fine sediments will be removed over time (Huisman et al., 2018), the PHZD has virtually unlimited supply of fine sediments situated within the core of the nourishment. It is expected that the storm event caused input of fine sediments from below the armour layer into the system. This is because the morphological change observed from 30 September to 2 October (Fig. 18) shows an erosion scarp above 0.3 m NAP (top picture Figure 3) with the fine sediments clearly visible below the coarse layer. Furthermore, visual observations of a layer of fine sediment deposited on the lower intertidal beach substantiate that as shown on the picture in Figure 3. This is also supported by the fine sediments samples in Figures 22 and 23 after the storm, showing

a increase in fine sediments. However, the fine sediments could also be the result of long shore transport. It is unlikely that these fine sediments come from the platform as GPS measurements show an (very small) increase in bed level height on the platform (Fig. 18).

5.3 Conceptual model for morphological development

The combination of the conceptual beach states and the important processes for sedimentary dynamics results in the conceptual model shown in Figure 31. During low energy conditions preferential transport can prevail which over time could result in reduced transport due to coarsening of the bed. Furthermore a steep profile was observed. During high energy conditions all the sediments could be mixed resulting increased availability of fine sediments. After these conditions a relative flatter profile was observed. The frequency of high energy events is thus important for the availability of the finer sediments. Together with the time it takes for all the fine sediment to be removed and the armour layer to develop, this determines the effectiveness of the protective wear layer. A low storm frequency with a fast armour layer development would result in an effective protective layer. A high storm frequency with slow armour layer development would imply fine sediments to be available for significant amounts of time reducing the effectiveness of the protective wear layer.

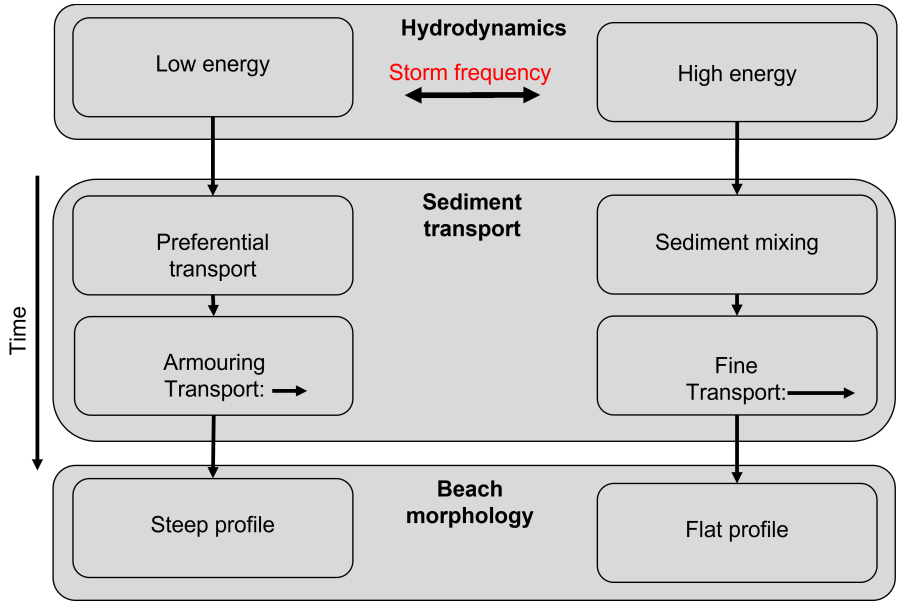

Figure 31: Conceptual model showing the roles of the important physical processes during different conditions.

As this is was not the first time a storm passed the PHZD and the profile flattened, it must be that between storm it steepens again. However, it was not observed how and during which conditions the flat profile transforms to a steep profile. It could be the result of erosion of mainly the fine sediments at the lower foreshore which results in steepening of the profile. Another possibility is the accretion of sediments above 0.3 m NAP by berm growth after an erosional event as shown in Figure 6. However, these hypothesis remain to be tested for the PHZD.

The availability of fine sediments is important for longshore transport. Due to flood dominance (Woerdman, 2022) the sediment is transported towards the end of the spit, which is extending (Fig. 32). The growth of the spit was expected from model simulations (Perk et al., 2019). However, the growth of the spit is going faster than expected. Model results showed that dredging at the mouth of the lagoon was necessary every 5 to 10 years (Perk et al., 2019). However, with the current rate of spit growth it could lead to dredging the mouth of the lagoon earlier than expected.

Figure 32: Longshore development over 2.5 years. Left: July 2019. Right: December 2021.

The longshore transport is under predicted. One reason for that could be the fact that Perk et al. (2019) used a tidal current of only 0.1 $\mathrm{m\,s^{-1}}$, while 0.2 – 0.4 $\mathrm{m\,s^{-1}}$ was measured, resulting in much lower longshore transport rates. Another reason could be that long term model simulations of Perk et al. (2019) include regular conditions and 15 storms in 5 years with a return period of 10 years. However, the monitored storm conditions only occurred at 7 Bft from an onshore direction for about 3 consecutive days. Considering the wind statistics at Texel, this happened 10 times in 2021 (Windguru,

2022). Even though sediment mixing and the availability of fine sediments is not included in the model, this could still result in an under prediction of the longshore transport.

5.4 Predicting sediment transport

The high scatter in both the prediction and measured sediment transport rates and turbidity shows that further calibration towards concentration is necessary. However, it doubtful how well that would work in this environment as it is known that OBS sensors are more sensitive to smaller grain sizes. Fugate and Friedrichs (2002) explain that OBS sensors actually measure the total grain cross-sectional area per unit area with no mass concentration in it. With this relationship to cross-sectional area in mind, Fugate and Friedrichs show the OBS is directly proportional to particle volume concentration and inversely proportional to the particle diameter. Hence the poor calibration for varying grain sizes, as on the PHZD. This raises the question what the OBS sensor is actually measuring.

The difficulty in measuring the suspended sediment transport and turbidity is illustrated by taking a look at Figure 27. During this storm period there are several peaks in concentration that correlate with peaks in shear stresses. After an energetic period in the morning of 29 September (waves of $\approx$ 45 cm), the conditions are much calmer for about a day. However, two large peaks (6 & 7) were observed during this calmer conditions. It is expected that this is not locally stirred sediment. A hypothesis is that fine sediment ($D_{50} < 100$ μm) is stirred somewhere else on the Wadden Sea, stayed in suspension long enough due to the very small grain sizes and passes the sensor due to the tidal flow. Pearson et al. (2019) found similar results at the Ameland tidal inlet and attributed it to organic sediment particles advected from the Wadden Sea. All this considered requires extra caution in interpreting the data, but also shows the difficulty for future calibration and it is questionable how well that will work.

5.5 Limitations and further research

There are several limitations in this study. One that is especially relevant is the sediment transport data that is not yet calibrated properly. It is necessary to not only calibrate the OBS sensors for sediment from the PHZD using the recirculation tank but also compare it to the Acoustic Backscatter Sensor (ABS) and ADV deployed at the same location. The method of Pearson et al. (2021) could then be used to differentiate between sand and mud.

There are also some limitations in the pressure and velocity data. These were collected at the same location, about 50 m offshore of the OBS and grain size samples (Section 3.2.2). The impact for waves is expected to be low (Fig. 15). For flow velocity this is yet unknown. Further processing of ADV data at L2C5 could greatly improve flow velocity data. At L2C5 the flow velocity is measured at three heights above the bed from which a critical flow velocity and velocity profile can be calculated. Furthermore it will give more insight of the the Total Kinetic Energy (TKE) at the beach step. This would be an interesting topic, which could possibly result in extra insights of sediment mixing depths under various conditions, which would be relevant for stirring and transport of sediments.

Further research on different minerals in armour layers is necessary. Heavier sediments are harder to mobilize and could function as a better armour layer (Koomans and De Meijer, 2004; Rafati et al., 2020). The carbonate content at the PHZD is relatively high. However, it should be further investigated how much this exactly is and what the impact is on sediment entrainment.

Furthermore, this study only focuses on one cross-shore profile only. However, the cross-shore profiles were not alongshore uniform (Fig. 10) and there is longshore hydrodynamic variability (J.B. Woerdman, 2022). Considering the findings of this study the longshore variability in morphology and transport should be further researched. The method of Quartel et al. (2008) compares the alongshore profiles and provides insight on the uniformity.

Lastly, the timing of physical processes should be evaluated. How fast are fine sediments removed from the bed and how does the profile steepen again. This is especially important for post storm processes and beach recovery. As Albert Einstein once said: "The only reason for time is so that everything doesn't happen at once".

6 Conclusions

This study at the Prins Hendrik Sand dyke substantiated some existing ideas and provided several new insights for sediment sorting and entrainment of complex sediment mixtures in a mixed wave-current environment. Below, the main conclusions are provided by addressing the research questions.

What is the sediment composition and how is it sorted?

What are the different sediment grain sizes?

There are three different modi of grain sizes found at L2. The smallest grain size was ~ 250 μm. The second modus is ~ 850 μm while the coarsest modus is ~ 2500 μm. This results in an average grain size including shells of all sediment samples collected at L2 during this campaign of 1032 μm. Shell (fragments) were responsible for a part of the larger grain sizes.

How is the cross-shore sediment sorting?

The sediment shows a slight fining in offshore direction from 1045 μm at L2C2 to 555 μm at L2C6. An exception is the beach step at the lower foreshore which is much coarser (1200 – 1300 μm) and consisted of a relatively larger amount of shells. The sediment is poorly sorted across the entire intertidal area ($\sigma_G = 2.3$ – 2.7).

How does the sediment sorting vary during different conditions?

The median grain size at the lower intertidal area was smaller during calmer conditions (430 – 860 μm) and larger during storm conditions (1350 – 2000 μm). It is unclear due to difference in preceding weather conditions, but our data suggest an overall coarsening during neap tide (880 to 1144 μm) as well as a higher positioned beach step.

What hydrodynamics drive the suspended sediment transport and how is this affected by the grain size distribution?

Is the stirring of sediment primarily wave- or tide-driven?

The sediment stirring is primarily wave driven as the Shields parameter is on average approximately 5 times bigger for waves (0.045) than for currents (0.0082). The steep slope in combination with larger waves during storm conditions can result in larger mixing depths. This results in large grain sizes possibly becoming entrained. Currents are especially important for sediment

transport. The current related shear stress only exceeds the critical shear stress for the D_{10}. However, in combination with waves the currents do contribute to more entrainment.

How does the mixed grain size mixture control the mobility of the sediment?

The mobility of the sediment at the intertidal beach of L2 is strongly influenced by the sediment composition. The mixed sediment composition causes differentiated entrainment which is counteracted by the hiding-exposure effect. The mobility of the smallest grains is reduced while larger grains are easier entrained. However, there was still preferential transport of fine sediments which over time causes some armouring due to the coarsening of the bed. The coarser bed reduced the mobility. Shell (fragments) in the sediment mixture also reduced the mobility of the sediment. The largest reduction in mobility was due to a thicker layer of shells. However, this was only very locally at the lower foreshore while most erosion occurred higher on the profile. During energetic conditions the entire bed could be mixed up which increased the availability of finer sediments. The conceptual model shows that storm frequency plays an important role in the availability of finer sediments.

How is the morphology shaped by the sediment composition?

The coarse sediment composition causes a relative steep beach profile with a beach step at the lower foreshore. However, after energetic conditions there is still a classical erosion profile with a rotation point at 0.3 m NAP causing a flattened beach profile. Additionally, the sediment mixture also enables preferential transport of fines as a result of which the spit is extending and built of relative fine sediments.

References

Aagaard, T. and Hughes, M. G. (2010), 'Breaker turbulence and sediment suspension in the surf zone', *Marine geology* **271**(3-4), 250–259.

Almeida, L., Masselink, G., Russell, P. and Davidson, M. (2015), 'Observations of gravel beach dynamics during high energy wave conditions using a laser scanner', *Geomorphology* **228**, 15–27.

Austin, M. J. and Buscombe, D. (2008), 'Morphological change and sediment dynamics of the beach step on a macrotidal gravel beach', *Marine Geology* **249**(3-4), 167–183.

Austin, M. J. and Masselink, G. (2006), 'Observations of morphological change and sediment transport on a steep gravel beach', *Marine Geology* **229**(1-2), 59–77.

Baba, J. and Komar, P. D. (1981), 'Measurements and analysis of setting velocities of natural quartz sand grains', *Journal of Sedimentary Research* **51**(2), 631–640.

Bagnold, R. A. (1946), 'Motion of waves in shallow water. interaction between waves and sand bottoms', *Proceedings of the Royal Society of London. Series A. Mathematical and Physical Sciences* **187**(1008), 1–18.

Bauer, B. O. and Allen, J. R. (1995), 'Beach steps: an evolutionary perspective', *Marine Geology* **123**(3-4), 143–166.

Bendixen, M., Clemmensen, L. B. and Kroon, A. (2013), 'Sandy berm and beach-ridge formation in relation to extreme sea-levels: A danish example in a micro-tidal environment', *Marine Geology* **344**, 53–64.

Berni, C., Perret, E. and Camenen, B. (2018), 'Characteristic time of sediment transport decrease in static armour formation', *Geomorphology* **317**, 1–9.

Blott, S. J. and Pye, K. (2001), 'Gradistat: a grain size distribution and statistics package for the analysis of unconsolidated sediments', *Earth surface processes and Landforms* **26**(11), 1237–1248.

Bosboom, J. and Stive, M. J. (2021), *Coastal dynamics*.

Brand, E., Ramaekers, G. and Lodder, Q. (2022), 'Dutch experience with sand nourishments for dynamic coastline conservation–an operational overview', *Ocean & Coastal Management* **217**, 106008.

Buijsman, M. C. and Ridderinkhof, H. (2007), 'Long-term ferry-adcp observations of tidal currents in the marsdiep inlet', *Journal of Sea Research* **57**(4), 237–256.

Buscombe, D. and Masselink, G. (2006), 'Concepts in gravel beach dynamics', *Earth-Science Reviews* **79**(1-2), 33–52.

Christensen, D. F., Hughes, M. G. and Aagaard, T. (2019), 'Wave period and grain size controls on short-wave suspended sediment transport under shoaling and breaking waves', *Journal of Geophysical Research: Earth Surface* **124**(12), 3124–3142.

De Bakker, A., Brinkkemper, J., Van der Steen, F., Tissier, M. and Ruessink, B. (2016), 'Cross-shore sand transport by infragravity waves as a function of beach steepness', *Journal of Geophysical Research: Earth Surface* **121**(10), 1786–1799.

Diedericks, G. P., Troch, C. N. and Smit, G. F. (2018), 'Incipient motion of shells and shell gravel', *Journal of Hydraulic Engineering* **144**(3), 06017030.

Dou, G., Dou, X. and Li, T. (2001), 'Incipient motion of sediment by waves', *Science in China Series E: Technological Sciences* **44**(3), 309–318.

Egiazaroff, I. (1965), 'Calculation of nonuniform sediment concentrations', *Journal of the Hydraulics Division* **91**(4), 225–247.

Elgar, S., Raubenheimer, B. and Guza, R. (2005), 'Quality control of acoustic doppler velocimeter data in the surfzone', *Measurement Science and Technology* **16**(10), 1889.

Elias, E., Cleveringa, J., Buijsman, M., Roelvink, J. and Stive, M. (2006), 'Field and model data analysis of sand transport patterns in texel tidal inlet (the netherlands)', *Coastal Engineering* **53**(5-6), 505–529.

Elias, E. P., Van der Spek, A. J., Wang, Z. B. and De Ronde, J. (2012), 'Morphodynamic development and sediment budget of the dutch wadden sea over the last century', *Netherlands Journal of Geosciences* **91**(3), 293–310.

Engelund, F. and Fredsøe, J. (1976), 'A sediment transport model for straight alluvial channels', *Hydrology Research* **7**(5), 293–306.

Ferreira, O., Ciavola, P., Taborda, R., Bairros, M. and Dias, J. A. (2000), 'Sediment mixing depth determination for steep and gentle foreshores', *Journal of Coastal Research* pp. 830–839.

Folk, R. L. and Ward, W. C. (1957), 'Brazos river bar [texas]; a study in the significance of grain size parameters', *Journal of sedimentary research* **27**(1), 3–26.

Fordeyn, J., Lemey, E. and Perk, L. (2020), 'A holistic approach to coastal protection for the prins hendrik polder', *Hydrolink* .

Foster, D., Bowen, A., Holman, R. A. and Natoo, P. (2006), 'Field evidence of pressure gradient induced incipient motion', *Journal of Geophysical Research: Oceans* **111**(C5).

Friedman, G. M., Sanders, J. E. et al. (1978), *Principles of sedimentology*, Wiley.

Fugate, D. C. and Friedrichs, C. T. (2002), 'Determining concentration and fall velocity of estuarine particle populations using adv, obs and lisst', *Continental Shelf Research* **22**(11-13), 1867–1886.

Gallagher, E. L., MacMahan, J., Reniers, A., Brown, J. and Thornton, E. B. (2011), 'Grain size variability on a rip-channeled beach', *Marine Geology* **287**(1-4), 43–53.

Gómez-Pujol, L., Jackson, D., Cooper, J., Malvarez, G., Navas, F., Loureiro, C. and Smith, T. (2011), 'Spatial and temporal patterns of sediment activation depth on a high-energy microtidal beach', *Journal of Coastal Research* pp. 85–89.

Goring, D. G. and Nikora, V. I. (2002), 'Despiking acoustic doppler velocimeter data', *Journal of hydraulic engineering* **128**(1), 117–126.

Grant, W. D. and Madsen, O. S. (1979), 'Combined wave and current interaction with a rough bottom', *Journal of Geophysical Research: Oceans* **84**(C4), 1797–1808.

Guillén, J. and Hoekstra, P. (1996), 'The "equilibrium" distribution of grain size fractions and its implications for cross-shore sediment transport: a conceptual model', *Marine Geology* **135**(1-4), 15–33.

Hassan, W. (2003), 'Transport of size-graded and uniform sediment under oscillatory sheet-flow conditions'.

HHN (2017), Prins hendrik zanddijk projectplan, Technical report.

Holland, K. and Elmore, P. (2008), 'A review of heterogeneous sediments in coastal environments', *Earth-Science Reviews* **89**(3-4), 116–134.

Huisman, B., De Schipper, M. and Ruessink, B. (2016), 'Sediment sorting at the sand motor at storm and annual time scales', *Marine Geology* **381**, 209–226.

Huisman, B., Ruessink, B., De Schipper, M., Luijendijk, A. and Stive, M. (2018), 'Modelling of bed sediment composition changes at the lower shoreface of the sand motor', *Coastal Engineering* **132**, 33–49.

Jennings, R. and Shulmeister, J. (2002), 'A field based classification scheme for gravel beaches', *Marine Geology* **186**(3-4), 211–228.

Knaeps, E., Moelands, R., De Keukelaere, L., Strackx, G. and Lemey, E. (2019), 'Mapping water quality with drones: test case in texel', *Terra et aqua* **157**, 6–16.

Komar, P. D. (1987), 'Selective grain entrainment by a current from a bed of mixed sizes; a reanalysis', *Journal of Sedimentary Research* **57**(2), 203–211.

Koomans, R. and De Meijer, R. (2004), 'Density gradation in cross-shore sediment transport', *Coastal engineering* **51**(11-12), 1105–1115.

Li, Y., Yu, Q., Gao, S. and Flemming, B. W. (2020), 'Settling velocity and drag coefficient of platy shell fragments', *Sedimentology* **67**(4), 2095–2110.

Madsen, O. S. and Grant, W. D. (1977), Quantitative description of sediment transport by waves, *in* 'Coastal Engineering 1976', pp. 1092–1112.

Masselink, G., Russell, P., Blenkinsopp, C. and Turner, I. (2010), 'Swash zone sediment transport, step dynamics and morphological response on a gravel beach', *Marine Geology* **274**(1-4), 50–68.

Masson-Delmotte, Zhai, P., Pirani, A., Connors, S. L., Péan, C., Berger, S., Caud, N., Chen, Y., Goldfarb, L., Gomis, M. I., Huang, M., Leitzell, K., Lonnoy, E., Matthews, J. B. R., Maycock, T. K., Waterfield, T., Yelekçi, O., Yu, R. and (eds.), B. Z. (2021), 'IPCC, 2021: Climate Change 2021: The Physical Science Basis. Contribution of Working Group I to the Sixth Assessment Report of the Intergovernmental Panel on Climate Change', *Cambridge University Press* .

McCarron, C. J., Van Landeghem, K. J., Baas, J. H., Amoudry, L. O. and Malarkey, J. (2019), 'The hiding-exposure effect revisited: A method to calculate the mobility of bimodal sediment mixtures', *Marine Geology* **410**, 22–31.

Miedema, S. A. and Ramsdell, R. C. (2011), 'Hydraulic transport of sand/shell mixtures in relation with the critical velocity', *Terra et Aqua* **122**(Mar), 18–27.

Mori, N., Suzuki, T. and Kakuno, S. (2007), 'Noise of acoustic doppler velocimeter data in bubbly flows', *Journal of engineering mechanics* **133**(1), 122–125.

Moss, A. (1963), 'The physical nature of common sandy and pebbly deposits; part ii', *American Journal of Science* **261**(4), 297–343.

Nielsen, P. (1992), *Coastal bottom boundary layers and sediment transport*, Vol. 4, World scientific.

Patel, S. B., Patel, P. L. and Porey, P. D. (2013), 'Threshold for initiation of motion of unimodal and bimodal sediments', *International Journal of Sediment Research* **28**(1), 24–33.

Pearson, S. G., Verney, R., van Prooijen, B. C., Tran, D., Hendriks, E. C., Jacquet, M. and Wang, Z. B. (2021), 'Characterizing the composition of sand and mud suspensions in coastal & estuarine environments using combined optical and acoustic measurements', *Journal of Geophysical Research: Oceans* p. e2021JC017354.

Pearson, S., van Prooijen, B., de Wit, F., Meijer-Holzhauer, H., de Looff, A. and Wang, Z. (2019), Observations of suspended particle size distribution on an energetic ebb-tidal delta, *in* 'Coastal Sediments 2019: Proceedings of the 9th International Conference', World Scientific, pp. 1991–2003.

Perk, L., van Rijn, L., Koudstaal, K. and Fordeyn, J. (2019), 'A rational method for the design of sand dike/dune systems at sheltered sites; wadden sea coast of texel, the netherlands', *Journal of Marine Science and Engineering* **7**(9), 324.

Poate, T., Masselink, G., Davidson, M., McCall, R., Russell, P. and Turner, I. (2013), 'High frequency in-situ field measurements of morphological response on a fine gravel beach during energetic wave conditions', *Marine Geology* **342**, 1–13.

Quartel, S., Kroon, A. and Ruessink, B. (2008), 'Seasonal accretion and erosion patterns of a microtidal sandy beach', *Marine Geology* **250**(1-2), 19–33.

Rafati, Y., Hsu, T.-J., Cheng, Z., Yu, X. and Calantoni, J. (2020), 'Armoring and exposure effects on the wave-driven sediment transport', *Continental Shelf Research* **211**, 104291.

Reed, C. W., Niedoroda, A. W. and Swift, D. J. (1999), 'Modeling sediment entrainment and transport processes limited by bed armoring', *Marine Geology* **154**(1-4), 143–154.

Reniers, A., Gallagher, E., MacMahan, J., Brown, J., Van Rooijen, A., Van Thiel de Vries, J. and Van Prooijen, B. (2013), 'Observations and modeling of steep-beach grain-size variability', *Journal of Geophysical Research: Oceans* **118**(2), 577–591.

Richmond, B. M. and Sallenger Jr, A. H. (1985), Cross-shore transport of bimodal sands, *in* 'Coastal Engineering 1984', pp. 1997–2008.

Rieux, A., Weill, P., Mouaze, D., Poirier, C., Nechenache, F., Perez, L. and Tessier, B. (2019), 'Threshold of motion and settling velocities of mollusc shell debris: Influence of faunal composition', *Sedimentology* **66**(3), 895–916.

Ruessink, B. (2010), 'Observations of turbulence within a natural surf zone', *Journal of Physical Oceanography* **40**(12), 2696–2712.

Shields, A. (1936), 'Application of similarity principles and turbulence research to bed-load movement'.

Slingerland, R. and Smith, N. D. (1986), 'Occurrence and formation of water-laid placers', *Annual Review of Earth and Planetary Sciences* **14**(1), 113–147.

Soulsby, R. (1997), 'Dynamics of marine sands'.

Soulsby, R. and Clarke, S. (2005), 'Bed shear-stress under combined waves and currents on smooth and rough beds (tr 137)'.

Soulsby, R. L. (1983), The bottom boundary layer of shelf seas, *in* 'Elsevier oceanography series', Vol. 35, Elsevier, pp. 189–266.

Soulsby, R., Whitehouse, R. et al. (1997), Threshold of sediment motion in coastal environments, *in* 'Pacific Coasts and Ports'97. Proceedings', Vol. 1, pp. 149–154.

Strypsteen, G., van Rijn, L., Hoogland, M., Rauwoens, P., Fordeyn, J., Hijma, M. and Lodder, Q. (2021), 'Reducing aeolian sand transport and beach erosion by using armour layer of coarse materials', *Coastal Engineering* **166**, 103871.

van der A, Dominic Ribberink, J. S., van der Werf, J. J., O'Donoghue, T., Buijsrogge, R. H., Kranenburg, W. M. et al. (2013), 'Practical sand transport formula for non-breaking waves and currents', *Coastal engineering* **76**, 26–42.

Van Rijn, L. C. (1993), *Principles of sediment transport in rivers, estuaries and coastal seas*, Vol. 1006, Aqua publications Amsterdam.

Van Rijn, L. C. (2007*a*), 'Unified view of sediment transport by currents and waves. i: Initiation of motion, bed roughness, and bed-load transport', *Journal of Hydraulic engineering* **133**(6), 649–667.

Van Rijn, L. C. (2007*b*), 'Unified view of sediment transport by currents and waves. ii: Suspended transport', *Journal of Hydraulic Engineering* **133**(6), 668–689.

Van Rijn, L. C. (2007*c*), 'Unified view of sediment transport by currents and waves. iii: Graded beds', *Journal of Hydraulic Engineering* **133**(7), 761–775.

Weir, F. M., Hughes, M. G. and Baldock, T. E. (2006), 'Beach face and berm morphodynamics fronting a coastal lagoon', *Geomorphology* **82**(3-4), 331–346.

Wiberg, P. L. and Sherwood, C. R. (2008), 'Calculating wave-generated bottom orbital velocities from surface-wave parameters', *Computers & Geosciences* **34**(10), 1243–1262.

Wilcock, P. R. and Crowe, J. (2003), 'A surface-based transport model for sand and gravel', *Hydraulic Engineering* **129**(2), 120.

Windguru (2022), 'Windguru archive'. `https://www.windguru.cz/archive-stats.php?id_spot=500859` [Accessed: 01.02.2022].

Winter, C. (2012), Observation-and Modelling of Morphodynamics in Sandy Coastal Environments, PhD thesis, Universität Bremen.

Wright, L. D. and Short, A. D. (1984), 'Morphodynamic variability of surf zones and beaches: a synthesis', *Marine geology* **56**(1-4), 93–118.

Zhu, Q., Van Prooijen, B., Wang, Z., Ma, Y. and Yang, S. (2016), 'Bed shear stress estimation on an open intertidal flat using in situ measurements', *Estuarine, Coastal and Shelf Science* **182**, 190–201.

Zuo, L., Roelvink, D., Lu, Y. and Li, S. (2017), 'On incipient motion of silt-sand under combined action of waves and currents', *Applied Ocean Research* **69**, 116–125.